



Changing Sea Level, Changing Shorelines: Comparison of Remote Sensing Observations at the Terschelling Barrier Island

Benedikt Aschenneller¹, Roelof Rietbroek¹, and Daphne van der Wal^{1,2}

¹Faculty of Geo-Information Science and Earth Observation (ITC), University of Twente, PO Box 217, 7500 AE Enschede, the Netherlands

²NIOZ Royal Netherlands Institute for Sea Research, Department of Estuarine and Delta systems, PO Box 140, 4400 AC Yerseke, the Netherlands

Correspondence: Benedikt Aschenneller (s.aschenneller@utwente.nl)

Abstract. Sea level rise is associated with increased coastal erosion and inundation. However, the effects of sea level change on the shoreline can be enhanced or counteracted by vertical land motion and morphological processes. Therefore, knowledge about the individual contributions of sea level change, vertical land motion and morphodynamics on shoreline changes is necessary to make informed choices when applying coastal defence measures. Here, we assess the potential of remote sensing techniques to detect a geometrical relationship between sea level rise and shoreline retreat for a case study at the Terschelling barrier island at the Northern Dutch coast. First, we find that sea level observations from satellite radar altimetry retracked with ALES can represent sea level variations between 2002 and 2022 at the shoreline when the region to extract altimetry timeseries is chosen carefully. Second, results for cross-shore timeseries of satellite-derived shorelines extracted from optical remote sensing images can change considerably dependent on choices made for tidal correction and parameter settings during the computation of timeseries. While absolute shoreline positions can differ on average by more than 200 m, the average trend differences are below 1 m yr^{-1} . Third, by intersecting the 1992 land elevation with time variable sea level, we find that inundation through sea level rise caused on average -0.3 m yr^{-1} of shoreline retreat between 1992 and 2022. The actual shoreline movement in this period was on average between -2.8 m yr^{-1} and -3.2 m yr^{-1} , leading to the interpretation that the larger part of shoreline changes at Terschelling is driven by morphodynamics. We conclude that the combination of sea level from radar altimetry, satellite derived shorelines and land elevation provides valuable information about the influence of sea level rise, vertical land motion and morphodynamics on shoreline movements.

1 Introduction

At the end of this century, global mean sea level is expected to rise by 0.56 m (middle-of-the-road scenario SSP2-RCP4.5) compared to the period 1986–2005 as computed in an ensemble-median projection of CMIP6 models (Hermans et al., 2021). In the Wadden Sea, projected sea level rise is close to global sea level rise with values between $0.41 \text{ m} \pm 0.25 \text{ m}$ (RCP2.6) and $0.76 \text{ m} \pm 0.36 \text{ m}$ (RCP8.5), derived from CMIP5 for the period 2018–2100 given as the 5–95% confidence interval (Vermeersen et al., 2018). Apart from saltwater intrusion, sea level rise also poses a higher risk of coastal hazards like floodings and storm surges, and has the potential to erode and inundate coastal areas. With an estimated global population of 267 million



25 people living in coastal areas below 2 m above mean sea level (Hooijer and Vernimmen, 2021), sea level rise is expected to lead to immense damage and costs for humanity and ecosystems (Hinkel et al., 2014; Schuerch et al., 2018). In order to enable timely and appropriate implementation of adaptation and defence strategies, it is therefore important to provide coastal zone managers and other coastal stakeholders with accurate information about current and expected sea level rise and its effect on shoreline movements.

30 Shoreline movements are not only caused by changes in sea level, but also by vertical land motion and morphological changes. Examples for morphological changes are sediment transports by currents, waves and wind, or sediment accumulation by vegetation. While sea level and vertical land motion are relatively well covered by observations from radar altimetry, tide gauges and GNSS (Global Navigation Satellite System), the complex morphodynamic contributions to shoreline changes and their feedback to rising sea levels are harder to quantify. More than five decades ago, Bruun (1962) first suggested a model
35 where with rising sea level sediment is displaced seaward along a profile, the so called Bruun Rule. Although the Bruun Rule is often criticised for using unlikely assumptions and missing the full complexity of morphological changes (e.g. Cooper and Pilkey, 2004), it still plays a substantial role in today's research of the link between sea level rise and shoreline retreat (e.g. Vousdoukas et al., 2020; D'Anna et al., 2021; Atkinson et al., 2018).

40 Here we suggest to use the available observations for sea level and vertical land motion in combination with estimates of shoreline changes to quantify the geometrical relation between sea level and shoreline changes. In contrast to the limited number of previous observational studies (Le Cozannet et al., 2014), we aim at developing a method based on remote sensing datasets that can potentially be applied globally in the future. In this paper, we assess the potential of remote sensing estimates for sea level and for shoreline changes by comparing them individually to complementary data sets covering the same processes,
45 and by combining them in order to study their interplay in terms of geometrical changes over a maximum time period of 30 years (1992–2022).

1.1 Sea surface heights

Sea level variations are observed with two techniques, locally with tide gauges and globally with satellite radar altimetry. Radar altimetry captures absolute sea level changes, the combined effect of mass- and volume changes relative to a reference ellipsoid.
50 In contrast, tide gauges register the relative sea surface heights from a station fixed to the ground, therefore these observations are also influenced by vertical land motion, including land subsidence and uplift. Vertical land motions can themselves lead to significant relative sea level changes (e.g. Pfeffer and Allemand, 2016; Santamaría-Gómez et al., 2012) and can be determined either directly using for example geodetic GNSS measurements, or indirectly, from the difference between relative sea surface heights from the tide gauges and absolute sea surface heights from satellite altimetry (e.g. Wöppelmann and Marcos, 2016;
55 Kleinherenbrink et al., 2018).



Retrieving altimetric sea surface heights in coastal areas is especially challenging. First, reflections from land in the altimeter footprint result in distorted signals, which require the application of specialised retracking algorithms to extract parameters such as the sea surface height. Second, the common geophysical and path delay corrections are not always available in the required temporal and spatial resolution to capture the small-scale processes near the coast. Retracking algorithms and corrections for coastal applications of satellite radar altimetry are continuously improved; currently, sea surface heights as close as 1-5 km to the coast can be retrieved (e.g. Birol et al., 2021; Vignudelli et al., 2019).

Satellite altimetry and tide gauges both observe sea level variations, but on different spatial and temporal scales. Tide gauges are almost exclusively installed on coasts and therefore lack spatial coverage, but they provide measurements with a high temporal resolution down to a few minutes (e.g. Holgate et al., 2013). On the other hand, satellite radar altimetry provides global coverage with a lower temporal resolution (e.g. Morrow et al., 2018; Vignudelli et al., 2011). The typical measurement frequency is about two to four observations per month, depending on the satellite's period of revolution around the Earth and the total number of altimetric satellites currently in orbit.

Despite these differences, observations from radar altimetry and tide gauges have been successfully combined for example to study the nearshore sea surface height changes due to strong currents, winds or bathymetry. Cipollini et al. (2017) compared non-retracked altimetry and tide gauge records at the coast of the UK by selecting matching pairs of observations in a radius of 0-200 km according to the smallest root mean square difference (RMSD). They found average correlations between 0.45 and 0.75 and RMSD values between 3.8 cm and 5.8 cm. Birol et al. (2021) did a similar study in six large coastal regions around the world and found an average correlation value of 0.77 for varying distances ($\sim 160 - 300$ km) to the respective tide gauges.

1.2 Shoreline positions

Shoreline positions can be observed in several ways, one of them being the extraction from optical satellite images. To be consistent with preceding literature, shorelines derived from optical satellite images are in this text referred to as satellite-derived shorelines. Various techniques have already been developed to compute satellite-derived shorelines in an automated fashion. A common approach is to use a classification procedure together with the computation of a spectral index such as the Normalized Difference Water Index (NDWI) to identify water and land pixels, and an edge-detection algorithm to define the border between these surfaces (e.g. Luijendijk et al., 2018; Vos et al., 2019b; Bishop-Taylor et al., 2021; Hagenaaers et al., 2018). Vos et al. (2019b) provide their methodology in the open-source CoastSat toolbox based on python and Google Earth Engine. Another freely available tool is CASSIE (Coastal Analyst System from Space Imagery Engine) by Almeida et al. (2021) which is also based on Google Earth Engine. Comparisons with in-situ surveys showed accuracies for satellite-derived shorelines between 10 and 30 m depending on the pixel resolution and the beach slope, assuming ideal conditions without clouds, waves or foam (Hagenaaers et al., 2018).



90 Another proxy for the shoreline position can be retrieved by intersecting a digital elevation model (DEM) with a plane at sea
surface height. The land elevation data are often gained with airborne laser altimetry (LiDAR) or photographs, and bathymetric
observations. When the DEM is available as gridded data, this can be done by extracting the contour line at sea level (e.g.
Parker, 2003). Often, land elevation data are distributed on profiles along cross-shore transects. The approach presented by
Stockdonf et al. (2002) uses linear regression to fit a function through the elevation data of a part of the profile, e.g. ± 0.5 m
95 around the shoreline, and evaluates this function at sea level. The error of this shoreline position compared to estimates from
GPS surveys was found to be between ± 1.1 m and ± 1.4 m, averaged over a stretch of 60 km (Stockdonf et al., 2002). This
approach is applied relatively often in the existing literature (e.g. Morton et al., 2005; Robertson et al., 2004), although usually
for a limited number of LiDAR overflights. Do et al. (2019) extracted shorelines derived from the yearly JARKUS dataset at
the Dutch coast over a period of 25 years. However, all applications so far focused on extracting the shoreline at one tidal
100 datum, for example at mean high water, without testing the influence of sea level changes on the shoreline position.

1.3 Study area

Terschelling is one of the barrier islands separating the North Sea from the Wadden Sea at the Northern Dutch coast (Fig. 1a).
The island is approximately 28 km long and 4 km wide. The amount of long-shore sediment transports is estimated to lie
between 0.8 and $1.2 \cdot 10^6 \text{m}^3/\text{yr}$ in eastern direction (Ridderinkhof et al., 2016). In the West and in the East of Terschelling,
105 the Vlie inlet and the Borndiep inlet connect the North Sea with the Wadden Sea. The coastal sections close to the inlets are
characterised by ebb tidal deltas with shoals, as well as a spit on the side of the Vlie inlet. We focus especially on the almost
straight northern sandy beach where there are no groynes, harbours or other hard, artificial structures. There was however one
shoreface nourishment carried out in 1993 (Brand et al., 2022).

110 Short-term sea level variations at Terschelling are dominated by diurnal tides with a tidal range of 1.2 m–2.8 m during neap
tide and spring tide, respectively. The average wave height is 1.5 m (Quataert et al., 2020). Terschelling houses two tide gauges,
one of them coupled to a GNSS station.

1.4 Linking shoreline change to sea level change

In this paper, we bring together observations of vertical sea level heights and horizontal shoreline positions to investigate the
115 geometrical influence of past and future sea level changes on shorelines. Additionally, we will compare estimates that describe
similar processes in order to illustrate the uncertainties in the underlying observations.

We start by evaluating the ability of offshore altimetry observations to capture sea level variations at the coast by comparing
altimetric sea level anomalies to sea surface heights from tide gauges (Sect. 3.1). The relative sea level from the tide gauges is
120 corrected for vertical land motion using the GNSS observations. A first result is then an altimetry timeseries that best represents
sea level at the coast. Furthermore, the northern sandy beach of Terschelling is covered by the JARKUS dataset providing yearly
observations of topographic and bathymetric heights along transects. By intersecting these profiles with a plane at sea level

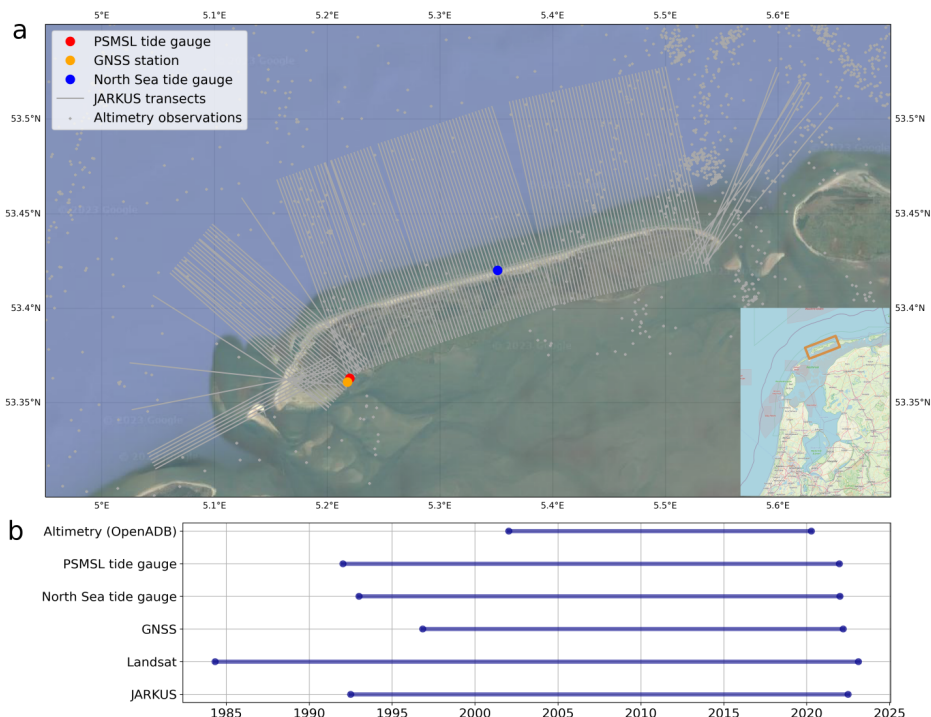


Figure 1. a: Locations of the PSMSL tide gauge coupled with the GNSS station, the North Sea tide gauge, the positions of the JARKUS transects and the closest of the offshore altimetry observations. Background image from Google Map tiles using cartopy.io.img_tiles (© Google Maps), inlay by OpenStreetMap (© OpenStreetMap contributors 2021). Distributed under the Open Data Commons Open Database License (ODbL) v1.0.). b: Time spans of the input data. For the two tide gauges and JARKUS we manually reduced the dataset to the period 1992–2022.

125 height we get an estimate of the shoreline position (Sect. 3.2). A second estimate for the shoreline position comes from optical remote sensing images, here we use the software CASSIE by Almeida et al. (2021) with Landsat satellite images (Sect. 3.3 and 3.4). We compare both shoreline estimates to validate them and to evaluate the achievable accuracy (Sect. 3.5). In order to be able to detect a possible geometrical connection between sea level rise and shoreline changes, we aim at studying long time periods. From the chosen datasets, the longest overlapping period covered is 2002–2020, limited by the retracked altimetry data distributed by the Open Altimetry Database (OpenADB) (Fig. 1b). An overview over the entire workflow is given in Fig. 2.

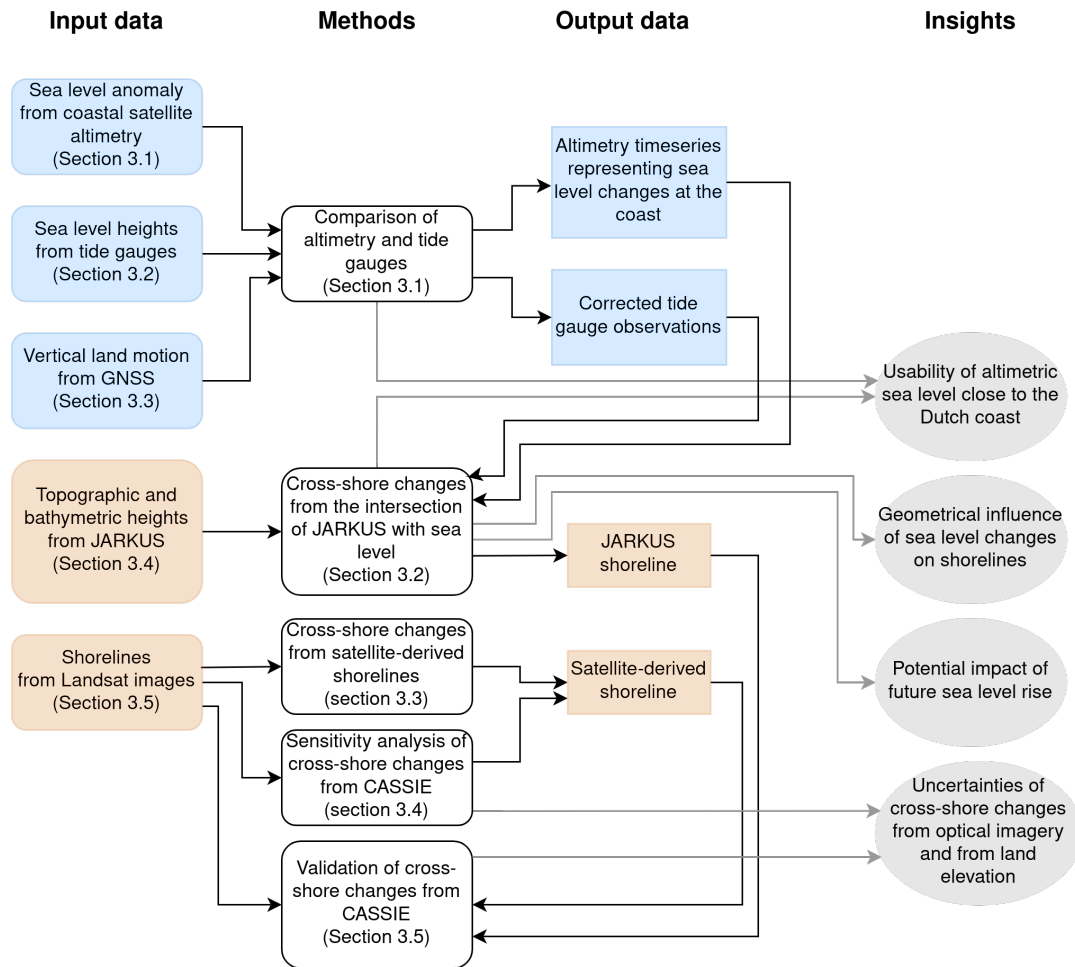


Figure 2. Workflow of this paper, with input and output data for sea level components in blue and for shoreline components in brown.

130 2 Data

2.1 Sea level anomaly from coastal satellite altimetry

We downloaded altimetric sea surface heights retracked with ALES (Passaro et al., 2014) in 1 Hz sampling rate from the Open Altimetry Database (OpenADB) (DGFI, 2023). Additionally to the ALES retracking, DGFI (2023) subjected this dataset to several pre-processing steps described in detail by (Oelsmann et al., 2021) and summarised in the following. First, the common
 135 corrections for path delay (wet and dry troposphere, ionosphere), as well as the geophysical corrections (atmospheric pressure, ocean tides, load tides, solid earth tides, pole tides, sea state bias) were applied. Details to the respective models used for the corrections can be found in (Oelsmann et al., 2021, Table 1). Second, sea surface heights from different satellite missions are cross-calibrated in a multi-mission crossover analysis. Third, the observations are interpolated on 1 Hz nominal tracks of the



140 respective missions. Fourth, outliers were removed, defined as observations where the sea level anomaly is larger than 2 m, where the difference of the respective observation to the running median over 20 points along track is larger than 12 cm or where the difference of two consecutive points along track is larger than 8 cm.

145 We downloaded sea surface heights retrieved from Envisat, Jason-1, -2, -3, SARAL and Sentinel-3A/B, in total covering the period 21.06.2002 – 12.04.2020. The extracted data covers an area of about 200 x 300 km North of Terschelling. Additionally to the above mentioned outlier rejection already done by DGFI, we excluded data points as recommended on the OpenADB website according to the following rules, (1) distance to coast < 3 km, (2) |sea level anomaly| > 2.5 m, (3) significant wave height > 11 m and (4) fitting error on the normalised leading edge (ALES) > 0.20 m. In the following, we continue to work with sea level anomalies derived by subtracting the mean sea surface from the instantaneous sea surface heights. Mean sea surface data from DTU18 (Andersen et al., 2018) is provided together with the OpenADB data.

150 2.2 Sea level heights from tide gauges

We use tide gauge data to assess the potential of satellite altimetry to determine long term sea level variability close to the coast. At Terschelling, observations from two tide gauges are available that differ in location and temporal resolution. From both data sets, we extract the period from January 1992 to December 2021.

155 The North Sea tide gauge (station Terschelling Noordzee, Rijkswaterstaat (2022b)) provides water levels at 10-minute resolution. For the comparison with altimetry, tide gauge data needs to be corrected for the response of the sea surface to atmospheric pressure changes (also called "inverted barometer correction" or "IB correction"). We compute the IB correction using the following relationship from Ponte (2006):

$$\eta^{ib} = -\frac{P_a - \bar{P}_a}{\rho g}, \quad (1)$$

160 where η^{ib} is the sea level change in response to the atmospheric pressure change, P_a is the local sea level pressure, the overbar indicates the spatial average over the entire ocean surface, ρ is the ocean density and g the gravitational acceleration. We use monthly mean sea surface pressure from the ERA5 atmospheric reanalysis (Hersbach et al., 2022) for P_a and the constants $\rho = 1027 \text{ kg/m}^3$ and $g = 9.80665 \text{ m/s}^2$.

165 Furthermore, the tide gauge observations have to be corrected for vertical land motion. We use the vertical component of GNSS observations (see Sect. 2.3) and directly subtract them from the tide gauge timeseries. This approach is possible as we aim not at comparing absolute sea surface heights between altimetry and tide gauge, and focus instead on the temporal variability. Before subtracting, the GNSS observations are interpolated to each time step of the tide gauge records. As the time period 01.01.1992–03.11.1996 is not covered by GNSS observations, we extrapolate the trend and seasonal signal of the available
170 GNSS observations back in time.



Additionally, the observations from the North Sea tide gauge in 10-minute resolution also have to be corrected for tides, for which we test several options:

- 175 1. The tidal models EOT20 (Hart-Davis et al., 2021) and FES2014 (Lyard et al., 2021), using the tidal prediction software from AVISO¹. The ALES altimetric sea surface heights from OpenADB were tidally corrected with FES2014. However, tide models have issues in shallow regions close to the coast (e.g. Piccioni et al., 2018), therefore we test other tidal corrections as well.
- 180 2. Butterworth filter with order = 3 and cut-off frequency = 30 days. The butterworth filter is a low-pass filter that causes almost no spurious oscillations in the time domain even with a reasonable sharp cut-off in the frequency domain (Roberts and Roberts, 1978).
- 185 3. T_Tide, a software to perform a harmonic analysis of the tidal signal to empirically determine the tidal correction from the observations. T_Tide was developed by Pawlowicz et al. (2002) for matlab, here we use the python version² that currently can only handle timeseries shorter than the period of the nodal tidal cycle of 18.6 years. We therefore compute the tidal correction from the first 5 years of the timeseries (01.01.1992 - 31.12.1996) and apply this correction to the entire period. For the harmonic analysis, the shallow water constituents are taken into account.

A second set of tide gauge data is available from the Permanent Service for Mean Sea Level (PSMSL). PSMSL distributes monthly averaged RLR (Revised Local Reference) data from a tide gauge in the harbour of West-Terschelling (station 23, Holgate et al. (2013)), adjacent to the Wadden Sea. We correct the PSMSL dataset for atmospheric pressure changes and for vertical land motion as described above for the North Sea tide gauge data. As this data set is already monthly averaged, we
190 assume that it does not contain any significant tidal signals.

2.3 Vertical land motion from GNSS

Observations of Vertical Land Motion (VLM), i.e., subsidence or uplift of the ground, are required to relate the relative sea level variations from the tide gauges to the absolute sea level variations from altimetry. We obtained observations of VLM from a permanent GNSS (Global Navigation Satellite System) station situated in the harbour of Terschelling (documented by Delft
195 (2022)), close to the PSMSL tide gauge. This GNSS station provides weekly measurements starting on 03.11.1996 until today. We use the solution processed by the Nevada Geodetic Laboratory (NGL14) (Blewitt et al., 2018) and distributed by SONEL (SONEL, 2022) as this solution has the largest coverage over the entire operating period back to November 1996.

The GNSS time series contains discontinuities from antenna and receiver changes. The respective dates are documented
200 on the station's website (Delft, 2022). We estimate the magnitude of the offsets by fitting a step function in a least squares adjustment to the timeseries, where each interval covers the period between two instrumental changes. Most offsets have a

¹<https://github.com/CNES/aviso-fes>

²https://github.com/moflaher/ttide_py



magnitude in the order of 1-2 mm which corresponds to the achievable accuracy of long term GNSS measurements. Therefore, not every estimated offset is necessarily significant, and not every instrumental change leads to a discontinuity in the time series (Fig. A1). Taking all offsets into account would lead to over segmentation and would eliminate the long term physical signal.

205 Determining which offsets are significant is a more or less subjective choice. Gazeaux et al. (2013) asked several groups to estimate time and magnitude of offsets in a simulated dataset. They found that from the variety of techniques applied, manual methods yielded overall better results than automated methods.

Here, we decide to manually remove one, two or three of the bigger offsets (with 9 mm, 4.5 mm and 3.8 mm respectively)

210 in order to get a time series clean of artificial jumps but still containing the signal of VLM. The resulting VLM rates are summarised in Table 1, together with estimates from other publications for the same GNSS station. These estimates cover slightly different time periods, but when assuming that VLM rates are stable over approximately four years, we see a rather wide spread between $-0.18 \pm 0.11 \text{ mm yr}^{-1}$ (Gravelle et al., 2023, ULR7A) and $-0.63 \pm 0.43 \text{ mm yr}^{-1}$ (Shirzaei et al., 2021). We continue to work with the VLM timeseries that results from removing the two largest offsets (version 2), as its VLM rate of

215 -0.50 mm yr^{-1} fits best in the range of estimates from earlier publications.

There are several possible causes for this small rate of subsidence. Natural causes comprise glacial isostatic adjustment, however this trend was reported to be slightly positive over the Wadden Sea (Simon et al., 2018). Another reason could be sediment compaction, where only the layer between the base of the GNSS station and the ground leads to a vertical movement

220 of $-4.1 \pm 1.8 \text{ mm yr}^{-1}$ at the Terschelling GNSS site (Karegar et al., 2020). Movement in this layer is not observed by direct GNSS observations, but the overall layer susceptible to compaction continues about 16 m beneath the base of the GNSS station. Potential anthropogenic causes could be gas extraction from a small gas field in West-Terschelling and several gas fields in East-Ameland, as well as a salt extraction field on the other side of the Wadden Sea in Haveland (Fokker et al., 2018).

Source	Period	VLM rate in mm yr^{-1}
This paper, original time series with all discontinuities	11/1996–03/2022	-1.15
This paper, version 1: Removing 9 mm-offset	11/1996–03/2022	- 0.69
This paper, version 2: Additionally removing 4.5 mm-offset	11/1996–03/2022	-0.50
This paper, version 3: Additionally removing 3.8 mm-offset	11/1996–03/2022	-0.40
NGL14 (Blewitt et al., 2016)	11/1996–03/2022	-0.57 ± 0.41
ULR7A (Gravelle et al., 2023)	01/2000–12/2020	-0.18 ± 0.11
Shirzaei et al. (2021)	10/1996–10/2019	-0.63 ± 0.43

Table 1. Summary of rates of vertical land motion found from the NGL14 dataset when removing one, two or three of the biggest offsets, in comparison to the results of other publications over different periods.



2.4 Topographic and bathymetric heights from JARKUS

225 We use land elevation data to intersect the beach height profile with sea level as a proxy for the shoreline. The Dutch coast
is covered by yearly observations of height profiles above and below water carried out by the Dutch Ministry of Infrastruc-
ture and Water Management (Rijkswaterstaat) since 1965. These measurements relative to NAP (Normaal Amsterdams Peil)
are provided through the JARKUS dataset (JAaRlijke KUSmeting, "Annual Coastal Measurement") (Rijkswaterstaat, 2022a;
Pot, 2011; Minneboo, 1995). The data are provided along transects with a spacing of about 250 m–500 m (Minneboo, 1995;
230 Athanasiou et al., 2019) and a spatial resolution in cross-shore direction of 5 m. Terschelling is covered by 217 transects (see
Fig. 1). The orientation of the transects remains constant over time.

The height profiles are obtained from topographic and bathymetric measurements. The topography above the waterline was
until 1996 observed with airborne stereo-photogrammetry (Pot, 2011), and since 1996 with airborne laser altimetry (LiDAR).
235 The standard deviation of the LiDAR observations is estimated to lie between 10 and 15 cm (de Graaf et al., 2003). The
bathymetry below the waterline is observed with single- and multi-beam echo sounding from ships (Pot, 2011; Wiegmann
et al., 2002) to an extent where a depth of approximately 8 m below NAP is reached. Bathymetry observations are made during
high tide, while topography observations are made during low tide, resulting in an overlap area.

2.5 Shorelines from optical satellite images

240 In order to assess the potential of satellite-derived shorelines for studying long-term shoreline changes, we use one of the
available algorithms to extract shoreline positions from optical satellite images, CASSIE (Coastal Analyst System from Space
Imagery Engine, Almeida et al. (2021)). As CASSIE runs entirely on Google Earth Engine, it is not required to download the
images. The cloud computation makes CASSIE a good candidate for upscaling the methodology to a global application in the
future.

245

After image pre-processing, the CASSIE software first computes the NDWI (Normalised Difference Water Index) and cre-
ates a histogram of NDWI values for each pixel and for each image. Second, the pixels per image are classified by computing
the Otsu threshold from the histogram. By default, two classes (land, water) are used. For estuaries and other environments
where the distinction between land and water is not clear, it is possible to use a multilevel Otsu thresholding with three classes
250 (land, water, intertidal; water and intertidal are afterwards grouped together). Third, the features in the resulting binary image
are converted to polygons. The first intersection of a polygon with the transect is defined as the shoreline. Finally, the so found
shoreline contour is smoothed with a moving-average filter (Almeida et al., 2021).

When using CASSIE, data from multiple missions are available, i.e. surface reflectances from Landsat (5, 7, 8, 9) and
255 top-of-atmosphere reflectances from Sentinel-2 (Almeida et al., 2021). Here we choose to use only Landsat images due to con-
cerns about consistency when mixing surface and top-of-atmosphere reflectances. The analysis region is defined by an area of



interest that can be drawn or imported as a .kml-file. For the selection of images, we use the full available timespan 30.04.1984–22.02.2023 with a cloud cover of less than 50 %. Images where the beach is not visible due to clouds were manually removed from the selection. Next, the user has some control over the features detected as shorelines by defining a baseline and setting the spacing and extent of transects that are created automatically perpendicular to this baseline. This step is important, as CASSIE detects only shorelines that intersect with a transect. We experimented using different baselines and extent parameters, as well as choosing 2 or 3 Otsu thresholding classes. Our experiments showed better shoreline detection when using the settings for 3 classes, as it reduced the number of transitions between bare sand and vegetation detected as shorelines.

Besides using CASSIE, we also extracted satellite-derived shorelines for five years between 2015 and 2020 from CoastSat (Vos et al., 2019b). In CoastSat, the images are downloaded from Google Earth Engine and processed locally. The study area is therefore restricted by hardware storage size required to store the images, as well as by the recommendation to not request more than 100 km² at the same time to avoid slow processing. Additionally, we encountered a problem with the cloud masking that in the majority of images classified the beach as clouds and consequentially removed all information about shorelines. The cloud mask stems from the USGS quality assessment band computed with the CFMask algorithm. We tested switching the parameters that control the type of cloud that is masked, but were not able to achieve satisfying results. In the end, we deactivated cloud masking and manually classified the images for these five years according to their subjective usability for coastline detection.

3 Methodology

3.1 Comparison of altimetry and tide gauges

We compare the temporal variability of retracked offshore altimetry observations against the in-situ sea level measurements from the North Sea tide gauge and the PSMSL tide gauge. The goal is to find the altimetry timeseries that best represents the sea level changes at the shoreline over the 18-year period (January 2002–March 2020) available from OpenADB.

We build altimetry timeseries by dividing the area into 25 x 25 km cells and binning the OpenADB ALES retracked sea level anomalies into these cells. From each of the resulting timeseries, we remove outliers whose values exceed three times the standard deviation (3σ rule). Next, we compute monthly averages of altimetry observations weighted with the inverse of the distance per observation to the cell centre.

The monthly averaged altimetry timeseries per cell are then compared to both tide gauges, the monthly PSMSL tide gauge and the North Sea tide gauge. For the latter, we test three options for tidal correction (see Sect. 2.2). For consistency, the timeseries from the North Sea tide gauge used for comparison are interpolated onto the non-equidistant times of acquisition of the altimetry observations before monthly averaging. For each cell, the altimetry and tide gauge timeseries are compared by computing the linear correlation coefficient, RMSE (after subtracting the mean sea level per timeseries) and absolute linear



290 trends. From these statistics, we choose the grid cells where altimetry observations agree best with sea level recorded by a tide
 gauge directly at the coast and build one timeseries by monthly averaging all observations from these cells.

3.2 Cross-shore changes from the intersection of land elevation data (JARKUS) with sea level

We derive timeseries of cross-shore shoreline changes as the intersection of the JARKUS topographic and bathymetric height
 295 profiles along transects with a horizontal plane at sea surface height using functions from the JARKUS Analysis Toolbox
 (JAT) (van IJzendoorn, 2022). Several combinations of the two intersecting surfaces result in the six solutions for cross-
 shore timeseries summarised in Table 2. Comparing certain solutions allows us to study 1) the geometrical influence of sea
 level compared to morphodynamics on the shoreline evolution, 2) the potential of altimetric sea level changes to compute
 shoreline positions, 3) the geometrical effect of sea level changes due to atmospheric pressure on shoreline changes, and 4)
 300 the potential geometrical impact of future sea level rise (Table 3). We assess these questions by analysing trend differences,
 absolute differences and RMSE between the solutions.

Nr	Short name	JARKUS	Sea level
1a)	TG corrected	Time variable profile	Time variable sea level from PSMSL TG including corrections
1b)	TG uncorrected	Time variable profile	Time variable sea level from PSMSL TG without corrections
2)	Altimetry	Time variable profile	Time variable sea level from altimetry
3)	Constant sea level	Time variable profile	Constant sea level = 0 m NAP
4a)	Constant profile (past)	Constant profile	Time variable sea level from PSMSL TG without corrections
4b)	Constant profile (future)	Constant profile	Time variable sea level from projection until the year 2100

Table 2. The combination of constant or time variable JARKUS profiles with constant or time variable sea level from the PSMSL tide gauge
 (TG) or from altimetry results in six solutions for timeseries of cross-shore change.

Solution difference	Insights
TG uncorrected (1b) - Constant profile (past) (4a)	Residual is the shoreline change due to morphodynamics
TG uncorrected (1b) - Constant sea level (3)	Residual is the shoreline change due to sea level change
TG corrected (1a) - Altimetry (2)	Usability of altimetry for shoreline analysis
TG corrected (1a) - TG uncorrected (1b)	Influence of sea level changes due to atmospheric pressure changes
Constant profile (past) (4a) - Constant profile (future) (4b)	Impact of future sea level rise

Table 3. Insights gained by differencing the solutions in Table 2.

To separate the geometrical effects of sea level and morphodynamics on the shoreline we either fix the JARKUS profile or
 sea level in time in order to compare these results against a version where both JARKUS and sea level are time variable. Fixing

sea level to a certain height results in shoreline changes only due to morphological processes. On the other hand, fixing the

305 JARKUS profile in time shows us the separated effect of sea level changes on shoreline evolution.

In order to learn to what extent the altimetric sea level anomalies extracted in Sect. 3.1 can be used to study shoreline evolution, we compute cross-shore timeseries with time variable sea level from the PSMSL tide gauge (TG) and from altimetry.

310 The tide gauge data has been corrected for vertical land motion and atmospheric pressure. To be consistent with JARKUS, the tide gauge data is yearly averaged, making tidal correction unnecessary. The observed vertical land motion is with approximately -0.5 mm yr^{-1} (see Sect. 2.3) small. Atmospheric pressure however was on average lower than the global mean pressure, leading to a bias in the yearly averaged IB correction between -1 cm and -4.5 cm (see Sect. 2.2) with the corrected sea level below uncorrected sea level. Therefore, we test the effects of the IB correction on the shoreline variability by computing
315 cross-shore timeseries from time variable tide gauge data with and without corrections.

Finally, the potential geometrical impact of future sea level rise in the theoretical absence of morphodynamics is assessed by intersecting a fixed JARKUS profile with projected sea level. We use a sea level projection for Den Helder from CMIP5 models as computed by Vermeersen et al. (2018), resulting in a cumulative sea level rise of $0.52 \pm 0.27 \text{ m}$ for the years 2018–2100
320 under RCP4.5. Here, we simplify the projected sea level rise to be linear assuming a constant rise of 0.62 cm yr^{-1} as we only look into long-term shoreline changes.

From the 217 JARKUS transects covering Terschelling, we removed 65 transects from the computation by thinning out the areas around West- and East-Terschelling where due to the curvature of the shoreline several of the provided transects cover
325 almost the same beach section. From the remaining 152 selected transects we only use the transects that provide at least 5 years of data between 1992 and 2022.

3.3 Cross-shore changes from satellite-derived shorelines

We compute timeseries of cross-shore changes by intersecting the shorelines extracted from optical satellite images using CASSIE and CoastSat (see Sect. 2.5) with the transect coordinates from JARKUS. The intersection computation is done with
330 functions from the CoastSat toolbox (Vos et al., 2019b). For the CASSIE-derived shorelines, we used the same 152 transects as for the JARKUS shorelines in Sect. 3.2. Using the JARKUS transects allows us to directly compare the CASSIE-derived shorelines against the JARKUS shorelines (see Sect. 3.5). The CoastSat estimates are limited to a region of 100 transects around the center of the coastline due to performance issues in larger areas.



335 As the satellite images are taken at different tidal stages we applied a tidal correction derived from the following relationship:

$$\Delta x = \frac{\Delta h}{\tan \beta}, \quad (2)$$

where Δx is the horizontal shift of the shoreline due to the difference Δh between the actual sea level at time of image acquisition and a reference sea level (here set to 0 m NAP) for a coastal section with beach slope $\tan \beta$. We use water levels
340 from the North Sea tide gauge and from the EOT20 tidal model, and interpolate them to the points in time of image acquisition. For the beach slope, we first compute the topography gradients from the JARKUS dataset and then take the median over all gradients along each transect in a certain buffer zone (in the following called "cross-shore buffer zone") around the shoreline position. This gives us an estimate of beach slope that varies in both spatial dimensions and in time. The horizontal shift Δx resulting from equation (2) can become unrealistically large, especially for small beach slopes. We therefore apply a threshold
345 of ± 100 m for the maximum tidal correction. The tidally corrected cross-shore timeseries are smoothed using a moving average filter with a window size of five observations that are non-equidistant in time.

3.4 Sensitivity analysis of cross-shore changes from CASSIE

A sensitivity analysis is carried out to quantify the influence of four parameters involved in the computation of cross-shore timeseries from CASSIE for the full available period 1984–2022. The goal is to get an idea of the uncertainty of the satellite-
350 derived shorelines and to make an informed choice of the parameter settings for further use.

Choices during the computation of intersections between shorelines and transects

First, the CoastSat function to compute the intersection between shorelines and transects offers the possibility to include a quality control procedure. This quality control applies for example thresholds for the standard deviation, the range and maximum values of the points involved in the computation, outlier rejection or the handling of several intersections along one
355 transect. We test the influence of using the function with or without quality control to compute the intersections. Second, this function actually computes several intersections per transect in a zone with a certain along-shore length, in the following called "along-shore zone". The median of these intersections is the final cross-shore position. Our second experiment is to test 13 values between 50 m and 2500 m for the length of the along-shore zone.

360

Choices for tidal correction

Third, the influence of using a tidal correction is investigated. We compare the use of no tidal correction, a tidal correction computed with a uniform beach slope (same beach slope for each transect and for each point in time) and the tidal correction using the variable beach slopes described in the previous section. For the latter, we use six cross-shore buffer zones along a
365 transect between ± 5 m and ± 105 m. Finally, we analyse the influence of the source of water levels where we compare the use of observations from the North Sea tide gauge against the use of sea level from the tidal model EOT20.



The results from each of these four experiments are one timeseries per transect and therefore two-dimensional. As a representative one-dimensional measure we compute the differences to the median of all timeseries per transect resulting from changing one of the parameters. Additionally, we look at the influence of changing these parameters on standard deviations and trends.

3.5 Validation of cross-shore changes from CASSIE

We validate the tidally corrected timeseries of cross-shore changes from CASSIE derived with the settings found in Sect. 3.4 by comparing them to two other datasets, satellite-derived shorelines from CoastSat using the same settings, and shorelines derived from the intersection of JARKUS with sea level. As means of comparison we compute the absolute differences, standard deviations, trends and correlations.

For the comparison with CoastSat, we have an overlapping period with CASSIE of five years between 2015 and 2020. The CASSIE-derived shorelines were extracted only from Landsat images, whereas in CoastSat we included additionally Sentinel-2 images. As a consequence, there are a total of 183 images used in CoastSat, but only 23 images in CASSIE when reduced to the same 5-year period.

For the comparison with the JARKUS-derived shorelines, we used the cross-shore changes resulting from the intersection with the uncorrected tide gauge (solution 1b), as this solution represents best the actual shoreline evolution. Temporal matching is done by interpolating the cross-shore positions from CASSIE with their irregular times of image acquisition on the yearly JARKUS time vector, covering the a period of 30 years from 1992 to 2022.

4 Results

4.1 Nearshore sea level variability from altimetry compared to tide gauges

In terms of correlations and RMSE aggregated over all cells, the timeseries of altimetric sea level anomalies show the best similarity with the PSMSL tide gauge with an average linear correlation coefficient of 0.53 and an average RMSE of 12.3 cm (Fig. 3). The comparison to the North Sea tide gauge corrected with EOT20 yields the second highest correlation coefficient with an average of 0.42 and the third lowest RMSE with an average of 19.3 cm. Almost the same results are achieved when correcting the tide gauge with FES2014 (not shown). Filtering the North Sea tide gauge data with a 30-day Butterworth filter leads to reasonable results with correlations around 0.4 and up to 0.6 and an average RMSE of 14.5, while correcting with the estimated tidal signal from T_Tide yields no significant correlation at all.

Creating altimetry timeseries from cells allows us to study the spatial distribution of correlation, RMSE and trend differences. As an example, the maps in Fig. 4 show the comparison of each altimetric sea level anomaly timeseries with the PSMSL

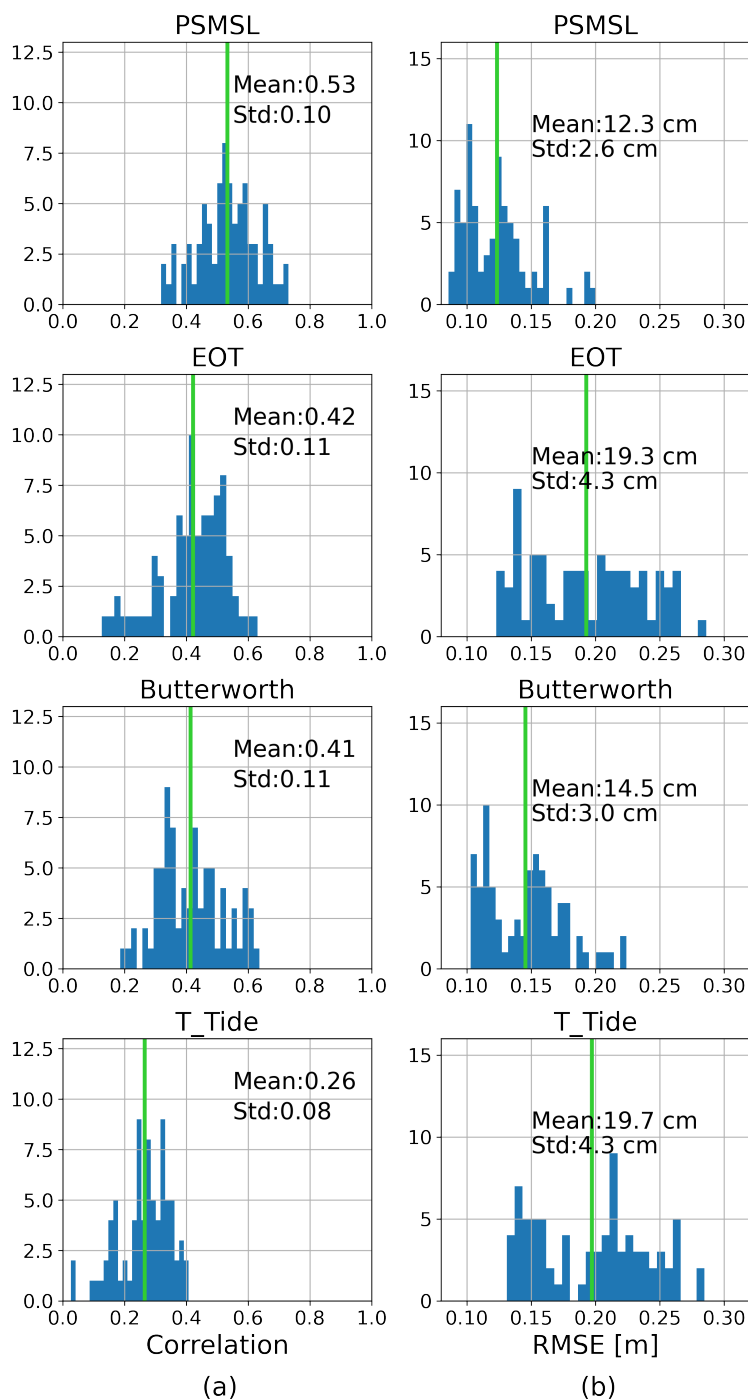


Figure 3. Histograms of linear correlation coefficients (a) and RMSE (b) between sea level anomalies altimetry and from tide gauges per cell for different tide gauge solutions, from top to bottom: Monthly PSMSL tide gauge without tidal correction, 10-minute resolution North Sea tide gauge corrected using the EOT tidal model, the North Sea tide gauge filtered with a 30-day Butterworth filter and the North Sea tide gauge corrected with T_Tide. The green vertical lines indicate the mean.

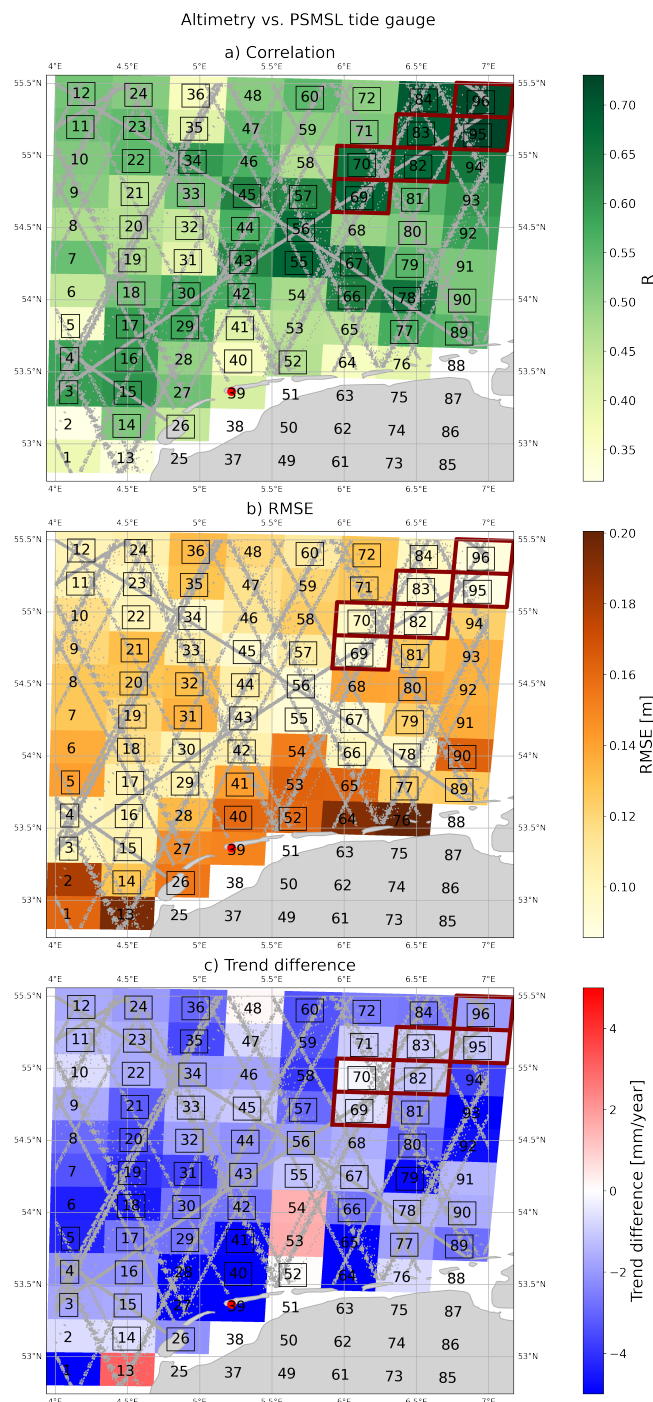


Figure 4. Maps of linear correlation coefficients (a) and RMSE (b) between sea level anomalies from altimetry and from the PSMML tide gauge per cell. (c) Map of differences between the linear trends from the altimetry timeseries and from the PSMML tide gauge. The numbers indicate the cell numbers. Cell numbers surrounded by a black box contain timeseries that cover at least the period 01.07.2002–31.03.2020. Cells surrounded by a red box are selected to create a timeseries of monthly altimetric sea level anomalies for further use.



400 tide gauge. There is a clearly visible pattern of higher correlation coefficients with values between 0.6 and 0.7 and lower RMSE with values between 9 and 11 cm in a wide cross over the tracks from the JASON satellites. Along these tracks, the altimetry timeseries cover the entire 18-year period, whereas timeseries in other locations are often significantly shorter.

Differencing the altimetric sea level trends with the trend from the PSMSL tide gauge results in a more scattered pattern. The absolute linear sea level trend for the period January 2002–April 2020 as observed by the PSMSL and the North Sea tide gauge is 4.7 mm yr^{-1} and 4.9 mm yr^{-1} , respectively. The differences between altimetry and PSMSL tide gauge are regularly in the order of magnitude of observed sea level trends. This is another indication that the nearshore altimetry measurements cannot always properly represent sea level variations at the coast. However, the differences along the JASON tracks are again smaller with values below 1.5 mm yr^{-1} .

410 The tide gauge data are corrected for atmospheric pressure using ERA5 data (see Sect. 2.2), whereas the altimetry data from OpenADB were corrected with the Dynamic Atmospheric Correction (DAC) by Carrère and Lyard (2003). However, when we apply the DAC to the tide gauge data, we find no similarity in terms of correlation and RMSE with the altimetry timeseries, mainly caused by two peaks in the DAC dataset that are not present in the altimetry dataset. Moreover, de-trending and de-seasoning the timeseries removed all correlations, therefore all similarities are caused only by the inter-annual signal.

415

For extracting an altimetry sea level timeseries for further use that is representative for sea level change at the shoreline we consider only the cells that cover at least the period 01.07.2002–31.03.2020 (213 months). From a total of 80 cells, this leaves 54 cells that contain a total of 125–220 months of data. The 10 best scoring cells in terms of linear correlation coefficient, RMSE and the trend difference to the PSMSL tide gauge in Table A1 indicate two regions as possible candidates. One lies in the North East of the studied region about 250 km away from the coast (cells 96, 95, 83, 82, 70, 69), the other one lies more in the center about 125 km away from the coast (cells 55, 67, 78). As correlation and RMSE are slightly better for the North East region (see Tables A2 and A3 for the statistics of both regions), we continue to work with a timeseries generated from these six cells. The resulting timeseries has an absolute linear sea level trend of 3.6 mm yr^{-1} for the period January 2002–April 2020.

4.2 Cross-shore changes from the intersection of JARKUS with sea level

425 The Terschelling shoreline exhibits retreating and advancing areas (Fig. 5). From these we select three sections, two on the outer retreating parts of the shoreline (sections A and C), and one on the central advancing part of the shoreline (section B). Larger trends appear in areas with mild beach slopes, while small trends are related to steeper parts of the beach (see Fig. A2).

Three examples of cross-shore timeseries resulting from the intersection computation for the solutions (1) - (4a) from each section are given in Fig. 6. The respective transects are indicated in Fig. 5. For these example transects, all of the solutions (1) - (3) with time variable JARKUS profiles show very similar shoreline changes. In contrast, solution (4) with the JARKUS

430

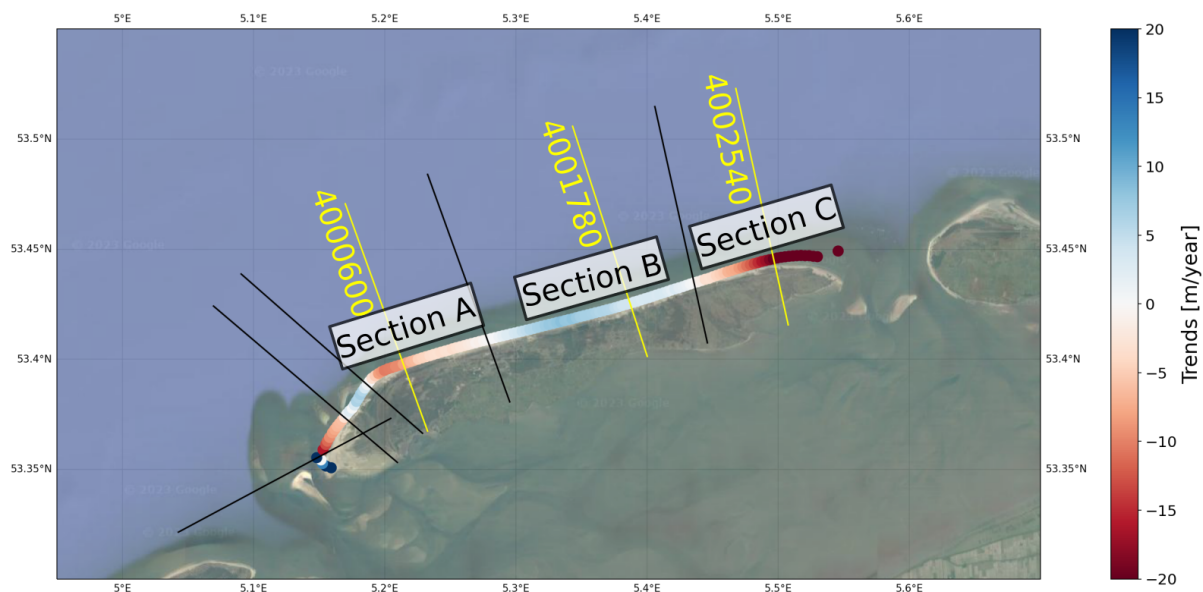


Figure 5. Trends of shoreline change derived from the JARKUS datasets differ along the coast of Terschelling, showing regions of seaward and landward movements. The trends shown here are computed by intersecting the profiles with the uncorrected PSMSL tide gauge (solution 1b). The black lines indicate the transects at the transitions between retreating and advancing sections of the coast. For the further analysis we focus on the two retreating sections A and C on the outer parts of the barrier island and the advancing section B approximately in the middle of the coastline. Furthermore, the transects used to extract the timeseries in Fig. 6 are shown in yellow. Background image from Google Map tiles using cartopy.io.img_tiles (© Google Maps)

profile fixed in 1992 does hardly show any visible shoreline variability.

In the following, we compare the shoreline trends from the different solutions from Tables 2 and 3 in terms of linear trends, absolute differences and RMSE. An overview of the statistics, averaged over the transects along the entire coastline and for the respective sections A, B and C, is given in the Tables 4 (trends), 5 (absolute differences) and 6 (RMSE). Overall, we find that the RMSE is always significantly larger than the respective absolute differences. It is therefore difficult to draw inclusions about an offset in absolute position between two compared shorelines. However, we can analyse the trend differences to answer the following questions:

440

What is the geometrical influence of sea level compared to morphodynamics on the shoreline evolution?

Under the assumption that the beach profile does not change over time (solution 4a), all sections respond with retreating shoreline trends. With magnitudes between -0.2 m yr^{-1} and -0.3 m yr^{-1} , inundation by sea level change is however rather small when compared to solution 1b) with time variable profiles where the landward trend in sections A and C ranges between -4.7

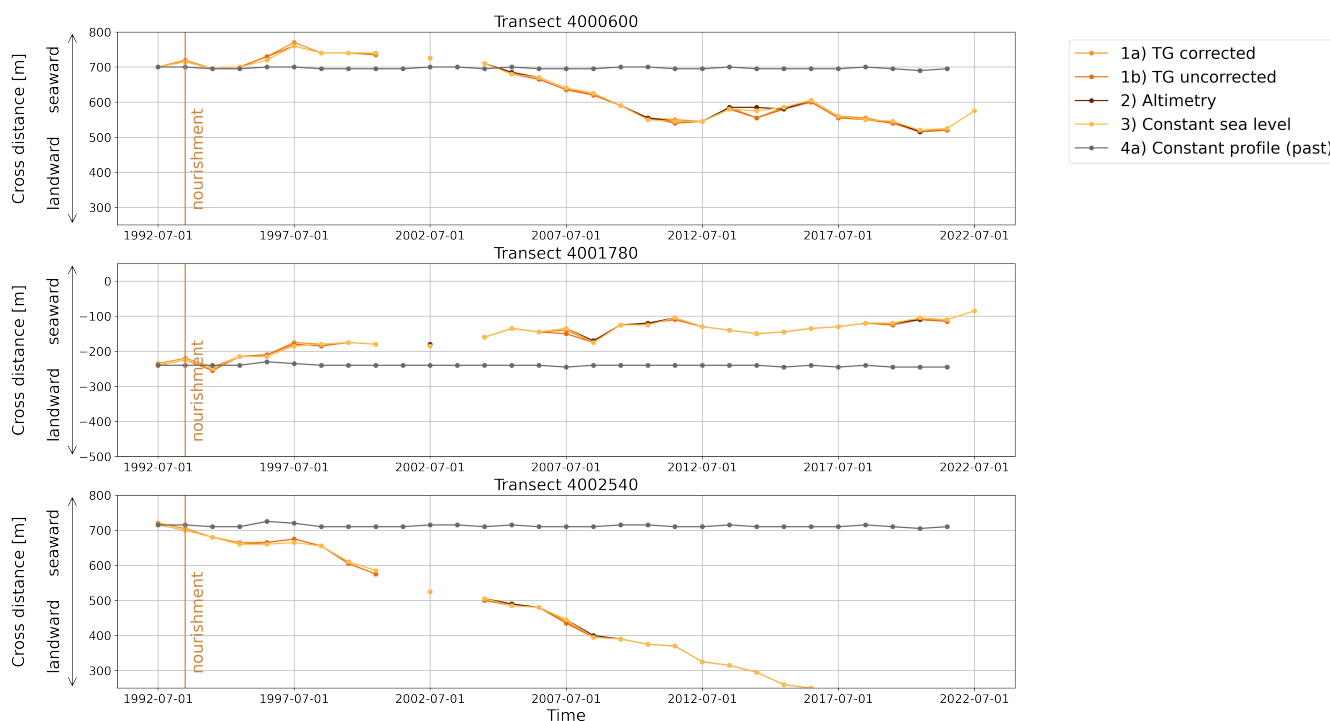


Figure 6. Three examples of cross-shore timeseries for the transects indicated in Fig. 5 showing landward trends in West and East Terschelling, and seaward trends for the central coast. The cross-distance on the y-axis is defined to point landward in the negative direction, while more positive values indicate a movement seawards. A negative trend therefore can be interpreted as a retreating shoreline, whereas a positive trend indicates an advancing shoreline. The absolute values depend on the definition of the coordinate system along the transects and can not be compared.

445 m yr^{-1} and -17.5 m yr^{-1} , respectively.

When comparing trends of shoreline changes resulting from variable sea level (1b) to the shorelines resulting from constant sea level 0 m over NAP (3) we find negative trend differences between -0.1 m yr^{-1} and -0.5 m yr^{-1} in all three sections. This indicates that timeseries from variable sea level (1b) exhibit on average more landward trends. However, when averaging over the entire coastline, the difference is with 0.4 m yr^{-1} positive, meaning that in the Western part of Terschelling (not included in the sections) the timeseries from variable sea level (1b) have larger seaward trends.

Can we use altimetric sea level changes to compute shoreline positions?

The trend differences between solution (1a) using the corrected PSMSL tide gauge and solution (2) using sea level from altimetry are always smaller than 0.1 m yr^{-1} . Consequently, exchanging the tide gauge data with an estimate based on altimetry



is justified.

To what extent do sea level changes due to atmospheric pressure alter shoreline changes?

When comparing the solution using the corrected PSMSL tide gauge (1a) to the uncorrected PSMSL tide gauge (1b), only section A exhibits a small trend difference of 0.1 m yr^{-1} . In terms of trends there is therefore no detectable difference induced by the correction for atmospheric pressure. We would expect a bias in shoreline position as the IB correction lowers the sea level by 1 to 4.4 cm, moving the shoreline seawards. This effect can be observed in the absolute differences ranging between 2.2 and 2.9 m, but due to the RMSE between 4.2 and 6.4 m a bias is not detectable with sufficient certainty.

What is the potential geometrical impact of future sea level rise?

We did the computation with the profile fixed in 1992 twice, first intersecting it with sea level from the uncorrected PSMSL tide gauge over the period 1992–2022, and second intersecting it with projected sea level over the period 1992–2100. For the three sections as well as for the entire shoreline, the landward trend increases for the 108 year period by $0.2\text{--}0.3 \text{ m yr}^{-1}$ compared to the 30 year period. The total estimated shoreline retreat between 1992 and 2100 averaged for the entire coastline is 32.4 m. The observed total shoreline change over the period 1992–2022 is -126.4 m for section A, 131.8 m for section B, -472.3 m for section C, and -97.1 m on average.

Trends [m yr^{-1}]	Entire coastline	Section A	Section B	Section C
1a) TG corrected	-3.2	-4.7	4.4	-17.5
1b) TG uncorrected	-3.2	-4.7	4.4	-17.6
1a) TG corrected, reduced to altimetry period	-2.8	-4.3	3.2	-16.2
2) Altimetry	-2.9	-4.3	3.2	-16.3
3) Constant sea level	-3.6	-4.4	4.5	-17.0
4a) Constant profile (past)	-0.3	-0.2	-0.3	-0.3
4b) Constant profile (future)	-0.5	-0.5	-0.5	-0.6
Trend differences [m yr^{-1}]				
TG uncorrected (1b) - Constant profile (past) (4a)	-2.9	-4.6	4.7	-17.2
TG uncorrected (1b) - Constant sea level (3)	0.4	-0.4	-0.1	-0.5
TG corrected (1a) - Altimetry (2)	0.1	0.0	0.0	0.1
TG corrected (1a) - TG uncorrected (1b)	0.0	0.1	0.0	0.0
Constant profile (past) (4a) - Constant profile (future) (4b)	0.2	0.3	0.2	0.3

Table 4. Trends and trend differences in m yr^{-1} for all investigated solutions described in tables 2 and 3, averaged over all transects along the entire coastline, and over the sections A (West), B (Center) and C (East). Time periods: 1992–2022 for solutions 1a)–1d), 3) and 4a, 2004–2021 for solution 2), 1992–2100 for solution 4b).



Absolute differences [m]	Entire coastline	Section A	Section B	Section C
TG uncorrected (1b) - Constant profile (past) (4a)	-36.1	-64.9	89.7	-234.5
TG uncorrected (1b) - Constant sea level (3)	-1.4	-1.2	-1.8	-1.4
TG corrected (1a) - Altimetry (2)	-0.5	-0.5	-0.6	-0.5
TG corrected (1a) - TG uncorrected (1b)	2.5	2.2	2.6	2.9

Table 5. Absolute differences in m between some of the solutions, averaged per transect over time and averaged over all transects along the entire coastline, as well as over the sections A (West), B (Center) and C (East).

RMSE [m]	Entire coastline	Section A	Section B	Section C
TG uncorrected (1b) - Constant profile (past) (4a)	153.2	91.1	104.4	284.4
TG uncorrected (1b) - Constant sea level (3)	5.6	4.4	5.9	5.5
TG corrected (1a) - Altimetry (2)	3.0	3.1	3.0	2.8
TG corrected (1a) - TG uncorrected (1b)	5.3	4.2	5.6	6.4

Table 6. RMSE in m for combinations of some of the solutions, averaged over all transects along the entire coastline, as well as over the sections A (West), B (Center) and C (East).

4.3 Sensitivity analysis of cross-shore changes from CASSIE

Choices during the computation of intersections between shorelines and transects

We first test the effect of computing intersections between shorelines and transects on the resulting cross-shore timeseries with or without the quality control implemented in CoastSat. In trends (Fig. 7) and in standard deviations (not shown), we find that using the function with quality control produces more stable results in the outer parts of the shoreline. These areas are characterised by ebb tidal deltas between the Wadden Sea and the North Sea with several shoals, spits and tidal flats (see Fig. 1) where probably several intersections are found. We therefore suspect that the function with quality control selects the intersections that belong to the main shoreline. When looking at the absolute differences between each timeseries (no quality control - with quality control) we find an average bias of -115.0 m, therefore the shorelines computed without quality control are on average further inland. However, this difference increases from -15.0 m to -226.5 m for along-shore zones from 50 m to 2500 m.

Second, when testing different values for the length of the along-shore zone, the timeseries with quality control have on average a higher variability with standard deviations up to 120 m, whereas the timeseries without quality control range around 80 m standard deviation (see Fig. A3). Average trends are with values between -1.7 m yr^{-1} and -2.0 m yr^{-1} more stable for the non-quality controlled timeseries, while the trends of quality controlled timeseries decrease considerably for along-shore zones higher than 1500 m up to -3.6 m yr^{-1} . The non-quality controlled timeseries are also more stable with regard to the

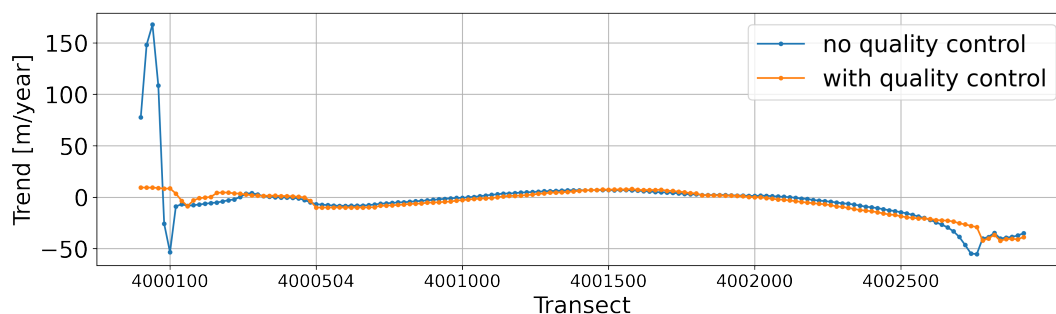


Figure 7. CASSIE shoreline trends for each transect from the CoastSat functions to compute the intersection between shoreline and transect without and with quality control. The length of the along-shore zone is here fixed to 1200 m. The six transects on the tip of the Western part of the island show strong deviations in the average trend in the non-quality controlled version that are not evident in the quality controlled version.

490 difference to the median of all solutions that reach a maximum of -1 m. In contrast, the differences of the quality-controlled timeseries show a linear decrease from 84.3 m to -67.5 m with the zero-crossing at 1250 m along-shore zone length.

We continue to compute the intersections with the quality control function as the cross-shore trends are more consistent along the shoreline. For the length of the along-shore zone we continue to work with 1200 m, making a trade-off between higher standard deviation but smaller difference to median, while keeping the trends at a reasonable magnitude.

495

Choices for tidal correction

The effect of using a tidal correction on the shoreline position is illustrated in Fig. 8 for the three example profiles that were earlier shown for the cross-shore changes from JARKUS in Sect. 4.2. Our third experiment is to test different tidal corrections, using a uniform beach slope with $\tan\beta = -0.01$ or using a variable beach slope (variable in along- and cross-shore direction, as well as in time) with cross-shore buffer zones between ± 5 m to ± 105 m around the shoreline position. The variability of the corrected timeseries is reduced by all tested types of tidal corrections to standard deviations (given as the median over all transects) between 87.5 m and 88.2 m, compared to 152.5 m for the uncorrected timeseries (see Fig. A4). Trends for the timeseries corrected with variable beach slopes vary between -0.4 m yr^{-1} and -1.2 m yr^{-1} , where larger cross-shore buffer zones tend to lead to larger trends. Using the uniform beach slope leads to seaward trends of -1.4 m yr^{-1} , using no tidal correction results in a trend of -1.6 m yr^{-1} . The difference to the median of all solutions is small with a maximum of 0.2 m for all tested tidal corrections with variable beach slopes, whereas the uniform beach slope leads to a deviation of 1.7 m. Not applying a tidal correction leads to a difference of -2.4 m. As applying a tidal correction reduces the standard deviation and the results are closer to the solution-median, we continue to work with the tidal correction using a variable beach slope with a 45 m cross-shore buffer zone.

510

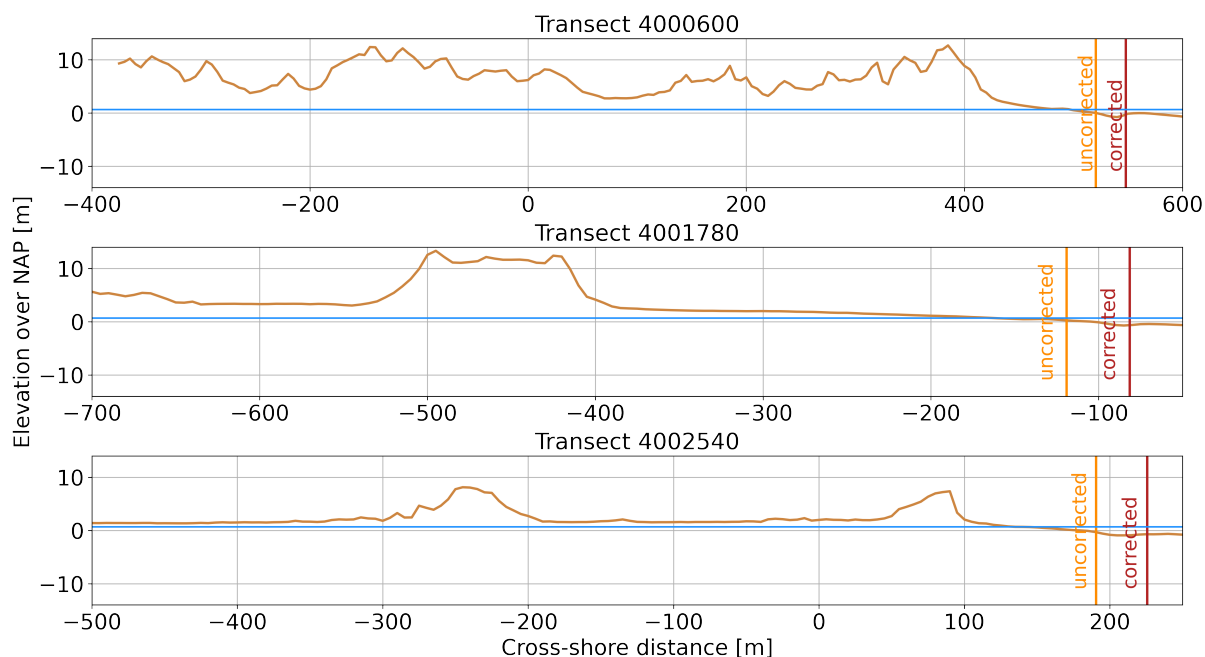


Figure 8. JARKUS profiles for the three example transects in Fig. 5 for the year 2020. The vertical lines indicate the CASSIE shoreline positions at 28.05.2020 10:32:54, without tidal correction (orange) and with tidal correction (brown). The tidal correction was computed using time- and space-variable beach slopes with a ± 45 m cross-shore buffer zone. The blue horizontal line indicates the water level (+67.7 cm) from the uncorrected North Sea tide gauge at the time of image acquisition. The reference sea level used for tidal correction is 0.00 m (see also Sect. 3.3).

Lastly, we compare the effect of using different sources of water levels for tidal correction, using measurements from the North Sea tide gauge and estimates from the EOT20 tidal model. When subtracting timeseries corrected with EOT20 from timeseries corrected with the tide gauge, we find differences that are almost constantly negative between -2.0 m and -14.3 m across all transects (Fig. A5). Consequently, the cross-shore changes tidally corrected with tide gauge observations are on average more landward than the timeseries using water levels from EOT20. These differences have a tendency to get larger towards the Eastern part of the shoreline. However, the source of water levels does not have an impact on the trends. We will continue to compute tidal corrections using the tide gauge observations.

4.4 Comparison of cross-shore changes from CASSIE and from CoastSat

When comparing standard deviations and trends per transect of cross-shore changes between CASSIE and CoastSat over the available 5-year period, the mismatch in sampling points with 23 images in CASSIE and 183 images in CoastSat manifests in large deviations for CASSIE over a wide part of the coast with standard deviations up to 200 m and trends down to -80 m yr^{-1} . These discrepancies in CASSIE do not appear over the entire 40-year period used in Sect. 4.3 where a single discontinuity in



the cross-shore timeseries has less impact. However, when we aggregate all absolute differences between both timeseries for all 100 transects covered by CoastSat in histogram (Fig. 9), we see a negative bias of -39.2 m on average. This result indicates that the CASSIE-derived shorelines have a tendency to lie further seaward than the shorelines extracted with CoastSat.

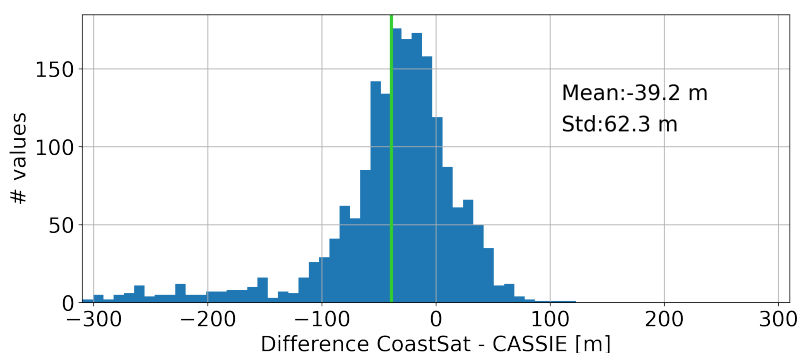


Figure 9. Histogram of absolute differences between the cross-shore timeseries from CoastSat minus CASSIE, both including tidal correction. The vertical green line indicates the mean. On average, shoreline positions derived with CASSIE are more landward compared to shorelines from CoastSat.

525

4.5 Comparison of cross-shore changes from CASSIE and from JARKUS

We assess the agreement between cross-shore changes extracted from Landsat images with CASSIE ("CASSIE-derived shorelines") and cross-shore changes computed as the intersection of JARKUS profiles with sea level ("JARKUS shorelines") in terms of their absolute differences, their standard deviations and trends, as well as the correlation per transect (Fig. 10). The absolute differences show a clear bias of -80.6 m on average where the CASSIE-derived shorelines are for the majority of the transects further seaward. The differences are larger for the outer transects in the western and eastern curvatures of the coastline.

In terms of standard deviations and trends, both methods to derive shorelines produce similar results. On average, the standard deviation of the JARKUS shorelines is 5.8 m smaller. However, the spatial pattern with a tendency to smaller standard deviations in the middle part of the coastline and larger variations in the outer parts is very similar. The trend differences show that JARKUS shorelines are on average by 2.1 m yr^{-1} more retreating, where the larger differences appear again in the two outer parts where beach slopes are mild. Areas with large trend differences are not related to areas with bigger or smaller seaward or landward trends (see Fig. 5). Along the central part of the shoreline where the beach slope is steeper, the differences in trends are usually below $\pm 2 \text{ m yr}^{-1}$.

540

Linear correlation coefficients between timeseries of CASSIE-derived shorelines and timeseries of JARKUS shorelines show an overall reasonable similarity with an average value of 0.55. In zones with large seaward or landward trends (see Fig. 5),

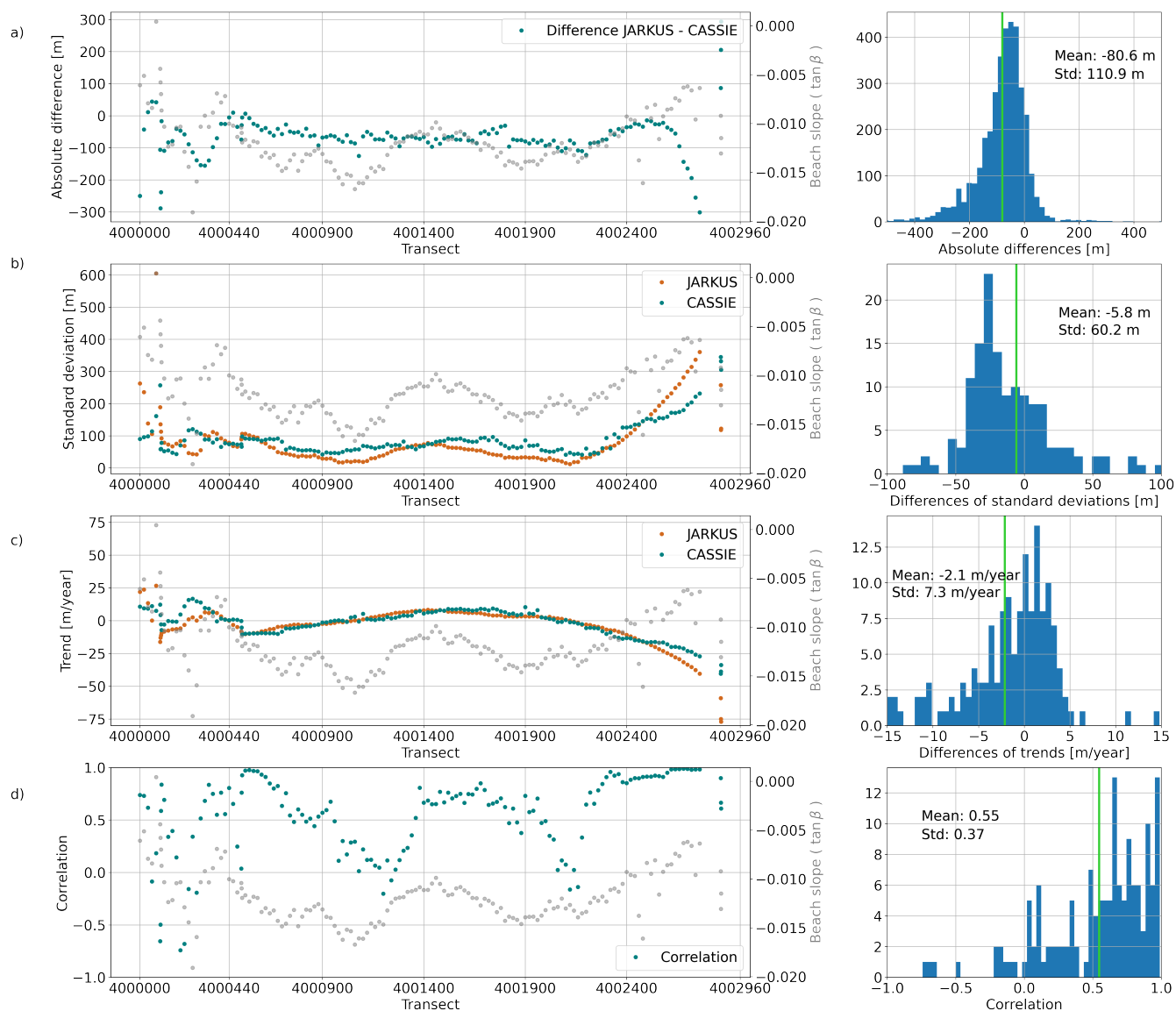


Figure 10. Statistics to compare timeseries of cross-shore changes from JARKUS and from satellite-derived shorelines extracted with CASSIE. a) Absolute differences JARKUS-CASSIE between the timeseries, as the median over each transect and as a histogram of all differences. b) Standard deviation per transect and histogram of differences of standard deviations (JARKUS-CASSIE). c) Trends per transect and histogram of trend differences (JARKUS-CASSIE). d) Linear correlation coefficient between CASSIE and JARKUS per transect and histogram of correlations. The vertical green lines in the histograms indicate the mean.



correlation reaches values above 0.70 and up to 0.99. Lowest correlations appear in the two stable zones, as well as in the Western curvature of the coastline.

545 **5 Discussion and conclusions**

A combined analysis of observational datasets describing sea level variations in relation to shoreline changes allows us to draw conclusions about the geometrical effect of long-term relative sea level changes and morphodynamics on shoreline movements at Terschelling. Furthermore, by comparing estimates that capture similar processes we can illustrate the uncertainties in the respective datasets.

550

Geometrical influence of sea level rise on shoreline changes

By intersecting topographic and bathymetric profiles from JARKUS data fixed in time with time-variable sea level we found that the observed 10.5 cm of relative sea level rise between 1992 and 2022 had a rather moderate impact on the shoreline evolution with an average landward trend of -0.3 m yr^{-1} . Instead, the observed shoreline movements were mainly associated with changes in the JARKUS profiles, leading to trends in shoreline position between -2.8 m yr^{-1} and -3.2 m yr^{-1} . From this we conclude that shoreline changes at the North Sea coast of Terschelling are currently largely driven by morphological processes, in this case erosion. For the Wadden Sea basin, Wang et al. (2012) showed that sedimentation rates compensate relative sea level rise. However, this equilibrium is likely to be disrupted when an unknown critical rate of sea level rise is reached (Wang et al., 2012). For a predicted total sea level rise of 0.52 m for the years 2018–2100 and under the assumption that there are no morphological changes, we find an average landward trend of -0.5 m yr^{-1} and a total shoreline change of -32.4 m for the North Sea coast of Terschelling. These values are relatively small compared to the changes in the observation period, but they are detectable. Additionally, erosion is known to be enhanced by sea level rise, for example leading to higher wave energy (e.g. D’Anna et al., 2021) and intensified tides (e.g. Jordan et al., 2021). Usually, relative sea level change by vertical land motion should be considered as well; however, in the case of Terschelling the observed VLM rates were below 1 mm yr^{-1} and had no detectable influence on the shoreline position.

560

565

Our computations were limited to the JARKUS transects with spacings of about 250 m. Additionally, the selection of transects that were used for the computation of the curved coastline of the eastern and western tip of the island was subjective. These issues could be resolved by using a gridded digital elevation model, if available, and applying image classification methods as was done for example by Liu et al. (2007) and Yousef et al. (2013). Additionally, the computation using the function from the JAT toolbox is limited by the JARKUS cross-shore resolution of 5 m, therefore the uncertainty for a single shoreline position can be up to $\pm 2.5 \text{ m}$. This could be improved by implementing a linear regression technique as presented by Stockdonf et al. (2002).

575



Usability of altimetric sea level anomalies at the coastline

In order to get the longest possible timeseries of altimetric sea level anomalies we combined observations from several altimetry missions in grid cells and assessed their similarity with the two tide gauges in terms of temporal variations dependent on the location of the grid cell. The overall similarity between altimetry and the PSMSL tide gauge is low expressed by correlation coefficients between 0.3 and 0.7, an RMSE between 0.09 m and 0.10 m and a median trend difference of 1.8 mm yr^{-1} , compared to previous studies (e.g. Mangini et al., 2022; Wöppelmann and Marcos, 2016; Cheng et al., 2012). However, the similarity between altimetry and tide gauges appears to have strong regional dependencies. Previous studies in the North Sea using various products (Dettmering et al., 2021; Birol et al., 2017; Cipollini et al., 2017) found maximum correlations of up to 0.8, 0.7 and 0.4 respectively, with decreasing values along the coasts of the Netherlands and France. In this context, we decided to extract an altimetry timeseries for further use from a field of approximately $50 \times 100 \text{ km}$ along the Jason tracks where correlation between altimetry and the PSMSL tide gauge ranges between 0.62 and 0.70, RMSE lies between 0.09 m and 0.10 m and trend differences are between -0.2 mm yr^{-1} and -1.9 mm yr^{-1} .

We observe that altimetric sea level anomalies have a tendency to become more representative of coastal sea level the further away they are from the coast. This phenomenon was reported in several earlier publications (e.g. Cazenave et al., 2022; Birol et al., 2017; Cipollini et al., 2017), and can be explained by the known problems of altimetry in the vicinity of the coast that require the use of retracking algorithms and specialised range corrections. An unexpected finding from our experiments is that the similarity is highest with the PSMSL tide gauge situated in the harbour in the Wadden Sea at West Terschelling. In contrast, the tide gauge at the North Sea coast is spatially closer to the altimetry measurements, but led to lower similarities for all tested tidal corrections. We also expected to see higher coincidence with a tide gauge timeseries corrected with the same tidal model that was used to correct the altimetry observations, FES2014. However, tide gauge timeseries corrected with FES2014 or EOT20 scored only second in terms of correlation and third in terms of RMSE, implying that global tidal models still can not capture significant tidal signals at the coast. A means of improvement might be to use the new regional tidal model EOT-NECS by Hart-Davis et al. (2023). Correcting the tide gauge by removing the observed tidal frequencies with T_Tide resulted in lowest correlations and second-lowest RMSE.

Replacing the tide gauge data in the shoreline computation from JARKUS with the extracted altimetry timeseries resulted in the same shoreline trends. We conclude that the uncertainties in the altimetric sea level anomalies do not hinder their use for shoreline analysis, which opens the possibility to study the influence of sea level on shorelines that are not covered by tide gauges.

Reliability of satellite-derived shorelines from CASSIE



610 For the extraction of shorelines from optical satellite images we mainly relied on the software CASSIE with Landsat im-
ages, yielding timeseries of cross-shore changes over 39 years between 1984 and 2023. Almeida et al. (2021) compared their
outcomes of CASSIE using Landsat 8 images to in-situ GNSS observations in one week during summer along four sandy
beaches in Brazil, and found with an RMSE of 8.84 m a similar range of uncertainties as previous studies of satellite-derived
shorelines. In order to learn more about the uncertainties of the CASSIE-derived shoreline timeseries at Terschelling, we tested
615 their sensitivity to tidal correction and parameters involved in the computation of timeseries. For validation, we compared
the CASSIE-derived shorelines to satellite-derived shorelines from the CoastSat toolbox by Vos et al. (2019b), as well as the
shorelines computed from the intersection of JARKUS with sea level.

When correcting the cross-shore positions for tides, we found that using a non-uniform beach slope that varies in along-
620 shore and cross-shore direction as well as in time considerably improved the results. Applying this tidal correction reduced the
temporal variability on average by up to 62 m and the difference to the median of all solutions by about 2 m compared to using
no tidal correction. Additionally, we saw an average trend increase by about 0.8 m yr^{-1} . We hypothesise that this difference
in long-term trends is caused by the sampling interval due to the sun-synchronous orbits of the Landsat satellites, leading to
aliasing of certain tidal frequencies (e.g. Eleveld et al., 2014; Bishop-Taylor et al., 2019).

625 Using a uniform beach slope that is constant in space and time, as was done in previous publications (e.g. Chen and Chang,
2009; Adebisi et al., 2021; ?; Vos et al., 2019a), reduced the standard deviation compared to using no correction but yielded
with 1.7 m a higher difference to the median of all solutions and higher trends. However, we only tested a single beach slope,
and the results could differ for other values. We conclude that especially for a coast with very mild beach slopes, it is preferable
630 to compute the horizontal shoreline shift due to tides with a space- and time-variable beach slope, although we realize that this
information is not always available.

Apart from the tidal correction, other parameters in the computation of cross-shore timeseries from satellite-derived shore-
lines showed their potential to alter the results considerably. For the upper and lower limit of the different tested settings, the
635 absolute shoreline position changed up to 226 m, while trends differed up to 1 m yr^{-1} . We expect that there are different best
settings for different sites, dependent for example on the degree of curvature of the shoreline or the presence of shoals and
other features that, from space, look similar to a shoreline.

Due to difficulties with cloud masking in the CoastSat toolbox, we only had results from a relatively short time period of
640 five years between 2015 and 2020 for a limited part around the central shoreline at hand. The comparison between CASSIE
and CoastSat showed large deviations in trends and standard deviations that can be mainly attributed to the low number of
Landsat images used in CASSIE in that period, increasing the impact of single outliers. We conclude therefore that trends from
the presented CASSIE-derived shoreline changes are only reliable over longer time periods. More insights might be gained
by including Sentinel-2 images in the CASSIE computation, however it should be tested before what the effect of combining



645 Landsat surface reflectances and Sentinel-2 Top-of-Atmosphere reflectances in one timeseries will be. While we cannot draw any conclusions about the uncertainties in shoreline trends due to the low number of images in the solution from CASSIE, we did observe a bias in absolute shoreline positions, where the CASSIE-derived shorelines are on average 39.2 m further seaward than the shorelines from CoastSat.

650 When comparing timeseries of CASSIE-derived shorelines with timeseries of JARKUS shorelines, we first note a bias of 80.6 m on average, where the CASSIE-derived shorelines are further seawards than the JARKUS shorelines. The linear correlation coefficients between both estimates are high with values between 0.70 and 0.99 in regions with higher landward or seaward trends, but reach also low and negative values below 0.50 in regions without a clear shoreline trend. Additionally, we found a difference in shoreline trends where the JARKUS shorelines were on average 2.1 m yr^{-1} more retreating with larger deviations
655 in the Eastern and Western parts of the shoreline. These outer parts are characterised by small beach slopes, a stronger shoreline curvature and additional seaward morphological features like shoals and spits, which hamper shoreline detection from satellite images. Our results are in line with the findings of Do et al. (2019), who compared tidally corrected satellite-derived shorelines from 13 Landsat images in the period 1985–2010 with JARKUS shorelines derived from the intersection with time variable sea level from a nearby tide gauge over a coastal section of 60 km south of Texel, the most southern Wadden island (see inlay
660 in Fig. 1). In terms of correlations between timeseries of Landsat and JARKUS shorelines, Do et al. (2019) find similar high values above 0.78 for certain zones. Although they too find a bias where the satellite-derived shorelines are further seawards, the magnitude of this bias is with 8 to 9 m on average about a factor 10 smaller than our result.

665 **Transferability to other sites**

The coast of Terschelling offers contrasting conditions, such as retreating and advancing areas, or a straight central shoreline and more complex configurations especially at the Western tip of the island. Nevertheless, the results concerning the impact of sea level rise on shoreline position will be different for other sites with different characteristics such as sediment material, tidal range or the shape of the shoreline. For example, protected "pocket-beaches" are more prone to inundation by sea level
670 rise than open beaches that suffer more from the increase in wave energy (Brunel and Sabatier, 2009). However, the methodology to determine the geometrical influence of sea level change and morphodynamics using land elevation data, altimetry and satellite-derived shorelines can in principal be applied to all sandy coasts. The main limitation is the availability of land elevation data in high spatial and temporal resolution with high accuracy. While such data are available locally (e.g., Aquitaine in France (Nicolae Lerma et al., 2022), Narrabeen beach in Australia (Turner et al., 2016), Duck in USA (Larson and Kraus,
675 1994)), global datasets that cover also countries with less financial means are much more scarce. For many coasts, the most accessible reference for long-term shoreline evolution comes therefore from satellite-derived shorelines. Finally, the observed shoreline and sea level changes at a prospective study site should exceed the uncertainty ranges in all data sets.



To conclude, our findings quantify the geometric interplay between coastal inundation by sea level changes and morpholog-
680 ical processes at Terschelling over the last three decades. The data-rich Dutch coast proved to be a valuable case study in that
we were able to illustrate uncertainties in the remote sensing data sets compared to the available in-situ and LiDAR data. This
paper provides a starting point to study the influence of sea level changes and morphodynamics in other regions, including
those which have less local datasets.

Code and data availability. The code used to produce the results of this paper is written entirely with open source python packages and can
685 be found in the github repository <https://github.com/3enedix/P1-data-combination-code.git>. Data produced in this paper can be found [in a](#)
[4TU.ResearchData repository https://data.4tu.nl/](https://data.4tu.nl/), to be created during publication.

Appendix A



A1 Cleaning GNSS height discontinuities

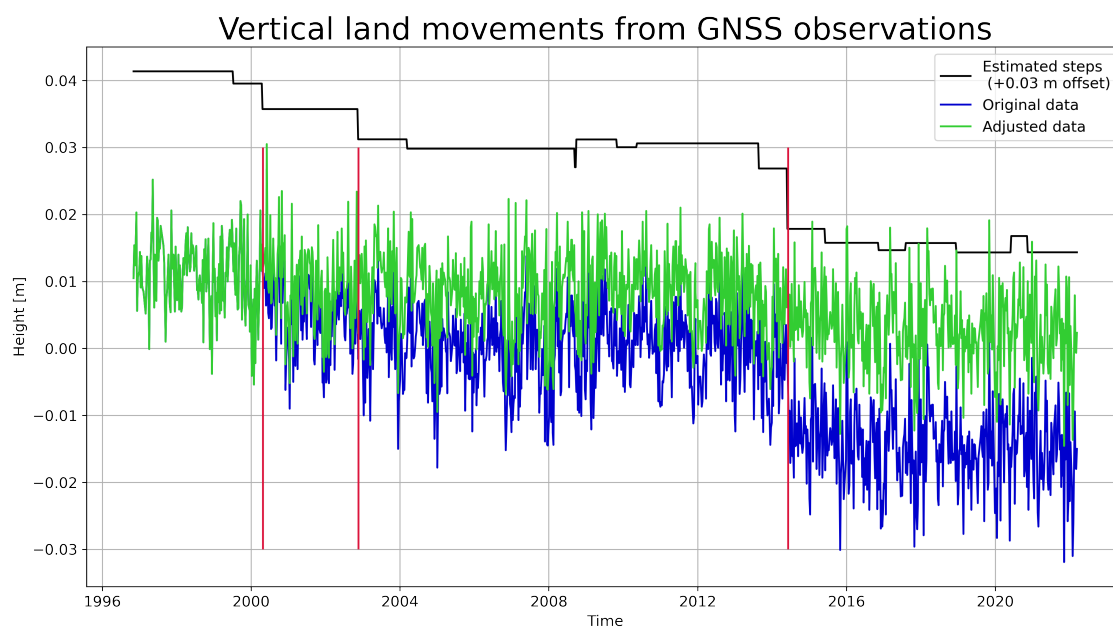


Figure A1. Vertical land motion from GNSS (NGL solution) at Terschelling. We estimate a step function with offsets for every indicated date of antenna or receiver changes. Most of these jumps are not significant. We therefore subsequently remove the three biggest offsets indicated by the vertical red lines. The green curve shown here is the result when removing all three offsets, resulting in a vertical land motion trend of -0.40 mm yr^{-1} .



690 **A2 Comparison of altimetric sea level anomalies against PSMSL tide gauge**

cell	R	cell	RMSE [m]	cell	trend difference [mm yr ⁻¹]
95	0.70	95	0.09	52	-1.1
83	0.67	83	0.09	70	-1.0
96	0.67	96	0.10	14	-1.9
84	0.64	55	0.10	78	-2.6
55	0.62	82	0.10	3	-1.2
82	0.62	67	0.10	77	-1.1
67	0.62	4	0.10	15	-1.3
78	0.61	69	0.10	44	-1.4
69	0.61	78	0.10	95	-0.6
15	0.59	56	0.10	69	-1.7

Table A1. Linear correlation coefficient R, RMSE and difference in linear trend between altimetry timeseries and the PSMSL tide gauge for the 10 best scoring cells, respectively.

cell	R	RMSE [m]	trend difference [mm yr ⁻¹]
96	0.67	0.10	-1.9
95	0.70	0.09	-1.1
83	0.67	0.09	-1.0
82	0.62	0.10	-1.1
70	0.66	0.10	-0.2
69	0.68	0.09	-0.6

Table A2. Linear correlation coefficient R, RMSE and difference in linear trend to the PSMSL tide gauge for the six cells forming the North East region.

cell	R	RMSE [m]	trend difference [mm yr ⁻¹]
55	0.62	0.10	-1.2
67	0.62	0.10	-1.4
78	0.61	0.10	-1.4

Table A3. Linear correlation coefficient R, RMSE and difference in linear trend to the PSMSL tide gauge for the three cells forming the middle region.

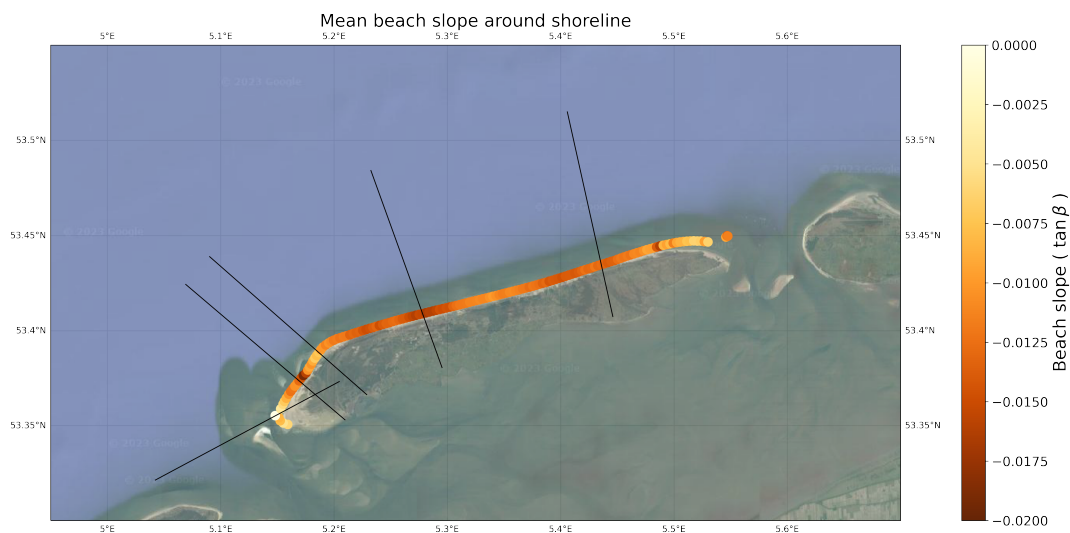


Figure A2. Mean beach slope per transect from the JARKUS data set. Beach slopes are especially mild at the outer parts that correlate with landward trends, and steeper to the middle of the coastline where the shoreline shows more seaward trends. The beach slopes in this figure are averaged in the area between the minimum and maximum shoreline position over the period 1992–2022. Background image from Google Map tiles using cartopy.io.img_tiles (© Google Maps)

A3 Beach slope in JARKUS

A4 Sensitivity analysis of cross-shore changes from CASSIE

Author contributions. BA led the conceptualization and methodology development of the study, conducted investigations and formal analysis, wrote the required software, validated and visualized the results and wrote the original draft. RR and DvdW aided in the conceptualization and methodology development, and supervised the research activities. All authors edited and reviewed the manuscript. No artificial intelligence tools have been used to help with the creation of text or code.

695

Competing interests. The authors declare that they have no conflict of interest.

Acknowledgements. This work made use of freely available data and software. The ALES SSH data were produced by DGFI-TUM and distributed via OpenADB (<http://www.openadb.dgfi.tum.de>). More details on the retracker and the product are available in Passaro et al. (2014), Passaro et al. (2015) and Passaro (2017). The data from Hersbach et al. (2022) used to compute the inverted barometer correction contain modified Copernicus Climate Change Service information 2020. The code used to compute FES2014 was developed in collaboration

700

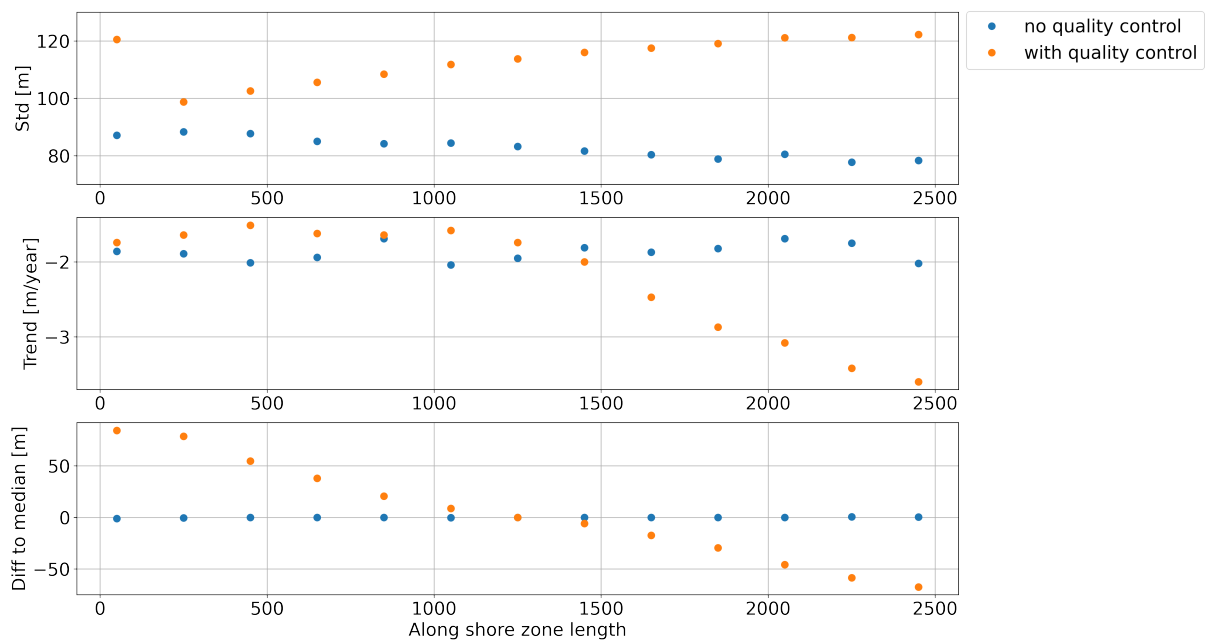


Figure A3. Sensitivity of satellite-derived cross-shore changes from CASSIE to changes in the along-shore zone length, the length of the zone used for the computation of one intersection between shoreline and transect. Presented are averaged statistics (standard deviation, trend and the difference to the mean of all solutions) for each solution computed as the median over all transects. An along-shore zone length between about 1000 m and 1500 m seems to be a reasonable choice with a small difference to median and stable trend estimates.

between Legos, Noveltis, CLS Space Oceanography Division and CNES, and is available under GNU General Public License (<https://www.aviso.altimetry.fr/en/data/products/auxiliary-products/global-tide-fes/description-fes2014.html>). Furthermore, we used the python packages CoastSat (Vos et al., 2019b), Jarkus Analysis Toolbox (JAT) (van IJzendoorn, 2022) and matplotlib (<https://doi.org/10.1109/MCSE.2007.55>).

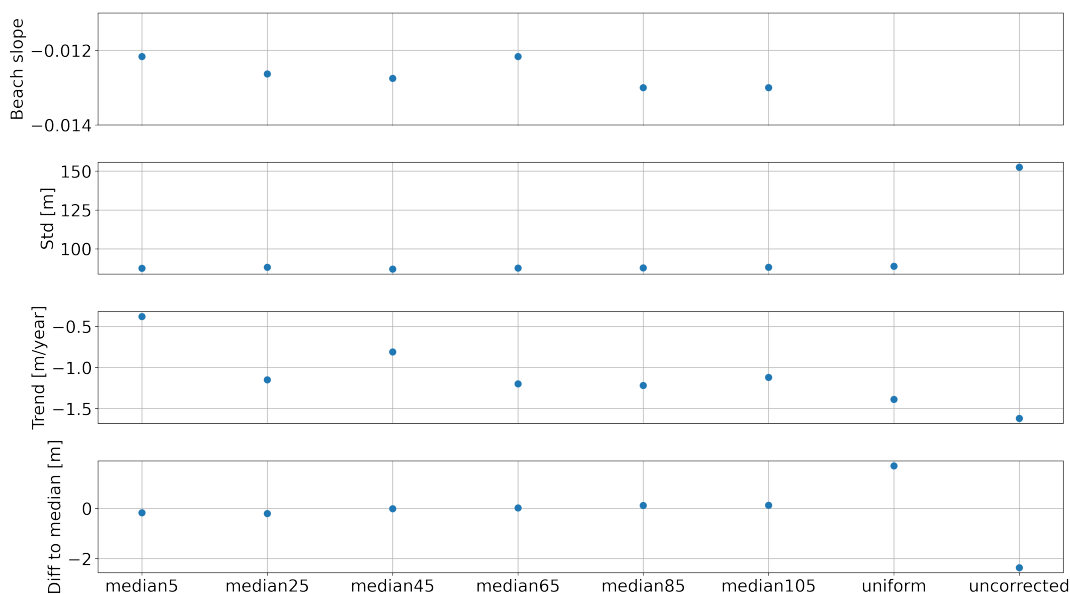


Figure A4. Sensitivity of satellite-derived cross-shore changes from CASSIE to different methods of tidal correction compared to using no tidal correction. 'median 5': Beach slope is computed as the median of all beach slopes in a buffer zone of ± 5 m around the shoreline position. We tested six buffer zone lengths between 5 m and 105 m. 'Uniform': One beach slope ($\tan\beta = -0.01$) for each transect and for each year. 'Uncorrected': No tidal correction. Statistics (standard deviation, trend and the difference to the mean of all solutions) are given as the respective median over all transects. The shown beach slope is computed as the median over time and the median per transect.

705 References

- Adebisi, N., Balogun, A.-L., Mahdianpari, M., and Min, T. H.: Assessing the Impacts of Rising Sea Level on Coastal Morphodynamics with Automated High-Frequency Shoreline Mapping Using Multi-Sensor Optical Satellites, *Remote Sensing*, 13, 3587, <https://doi.org/10.3390/rs13183587>, 2021.
- Almeida, L. P., Efraim de Oliveira, I., Lyra, R., Scaranto Dazzi, R. L., Martins, V. G., and Henrique da Fontoura Klein, A.: Coastal Analyst System from Space Imagery Engine (CASSIE): Shoreline Management Module, *Environmental Modelling & Software*, 140, 105033, <https://doi.org/10.1016/j.envsoft.2021.105033>, 2021.
- 710 Andersen, O. B., Nielsen, K., Knudsen, P., Hughes, C. W., Bingham, R., Fenoglio-Marc, L., Gravelle, M., Kern, M., and Polo, S. P.: Improving the Coastal Mean Dynamic Topography by Geodetic Combination of Tide Gauge and Satellite Altimetry, *Marine Geodesy*, 41, 517–545, <https://doi.org/10.1080/01490419.2018.1530320>, 2018.
- 715 Athanasiou, P., van Dongeren, A., Giardino, A., Vousdoukas, M., Gaytan-Aguilar, S., and Ranasinghe, R.: Global Distribution of Nearshore Slopes with Implications for Coastal Retreat, *Earth System Science Data*, 11, 1515–1529, <https://doi.org/10.5194/essd-11-1515-2019>, 2019.
- Atkinson, A. L., Baldock, T. E., Birrien, F., Callaghan, D. P., Nielsen, P., Beuzen, T., Turner, I. L., Blenkinsopp, C. E., and Ranasinghe, R.: Laboratory Investigation of the Bruun Rule and Beach Response to Sea Level Rise, *Coastal Engineering*, 136, 183–202, <https://doi.org/10.1016/j.coastaleng.2018.03.003>, 2018.
- 720

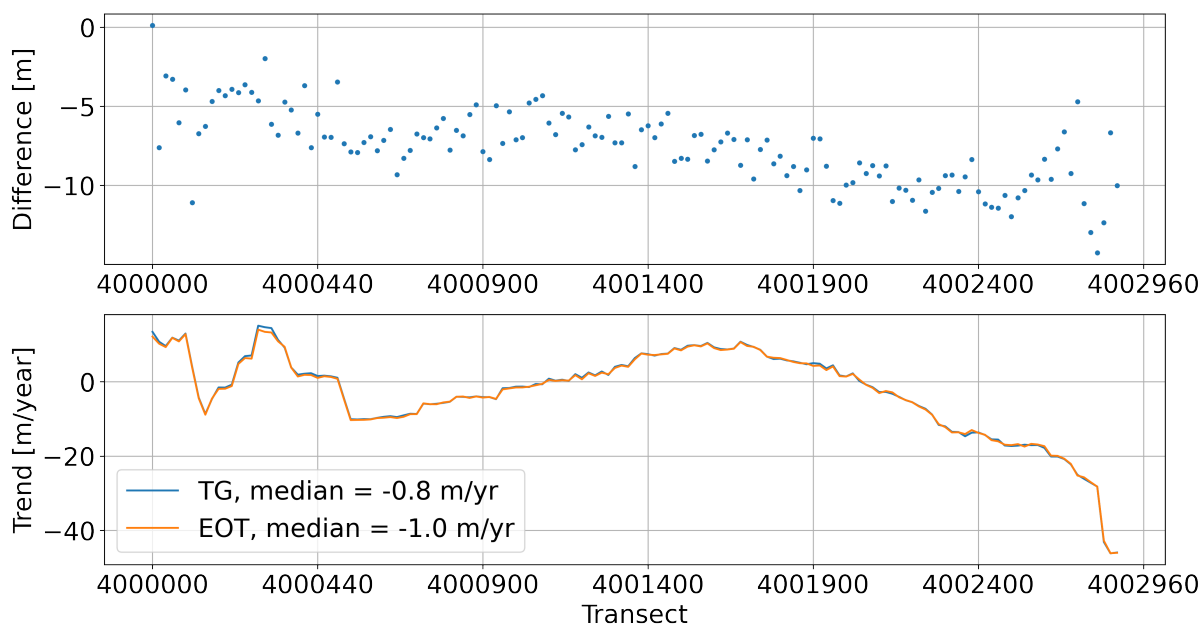


Figure A5. Sensitivity of tidally corrected cross-shore changes to the source of water level used for tidal correction. Upper: Median of absolute differences per transect between the cross-shore timeseries tidally corrected with water levels from tide gauge observations minus the version corrected using water levels from the EOT20 tidal model. Lower: Standard deviations of cross-shore timeseries tidally corrected with tide gauge data or EOT20.

- Birol, F., Fuller, N., Lyard, F., Cancet, M., Niño, F., Delebecque, C., Fleury, S., Toubanc, F., Melet, A., Saraceno, M., and Léger, F.: Coastal Applications from Nadir Altimetry: Example of the X-TRACK Regional Products, *Advances in Space Research*, 59, 936–953, <https://doi.org/10.1016/j.asr.2016.11.005>, 2017.
- 725 Birol, F., Léger, F., Passaro, M., Cazenave, A., Niño, F., Calafat, F. M., Shaw, A., Legeais, J.-F., Gouzenes, Y., Schwatke, C., and Benveniste, J.: The X-TRACK/ALES Multi-Mission Processing System: New Advances in Altimetry towards the Coast, *Advances in Space Research*, 67, 2398–2415, <https://doi.org/10.1016/j.asr.2021.01.049>, 2021.
- Bishop-Taylor, R., Sagar, S., Lymburner, L., and Beaman, R. J.: Between the Tides: Modelling the Elevation of Australia’s Exposed Intertidal Zone at Continental Scale, *Estuarine, Coastal and Shelf Science*, 223, 115–128, <https://doi.org/10.1016/j.ecss.2019.03.006>, 2019.
- 730 Bishop-Taylor, R., Nanson, R., Sagar, S., and Lymburner, L.: Mapping Australia’s Dynamic Coastline at Mean Sea Level Using Three Decades of Landsat Imagery, *Remote Sensing of Environment*, 267, 112 734, <https://doi.org/10.1016/j.rse.2021.112734>, 2021.
- Blewitt, G., Kreemer, C., Hammond, W. C., and Gazeaux, J.: MIDAS Robust Trend Estimator for Accurate GPS Station Velocities without Step Detection, *Journal of Geophysical Research: Solid Earth*, 121, 2054–2068, <https://doi.org/10.1002/2015JB012552>, 2016.
- Blewitt, G., Hammond, W., and Kreemer, C.: Harnessing the GPS Data Explosion for Interdisciplinary Science, *Eos*, 99, <https://doi.org/10.1029/2018EO104623>, 2018.
- 735 Brand, E., Ramaekers, G., and Lodder, Q.: Dutch Experience with Sand Nourishments for Dynamic Coastline Conservation – An Operational Overview, *Ocean & Coastal Management*, 217, 106 008, <https://doi.org/10.1016/j.ocecoaman.2021.106008>, 2022.



- Brunel, C. and Sabatier, F.: Potential Influence of Sea-Level Rise in Controlling Shoreline Position on the French Mediterranean Coast, *Geomorphology*, 107, 47–57, <https://doi.org/10.1016/j.geomorph.2007.05.024>, 2009.
- Bruun, P.: Sea-Level Rise as a Cause of Shore Erosion, *Journal of the Waterways and Harbors Division*, 88, 117–130, <https://doi.org/10.1061/JWHEAU.0000252>, 1962.
- 740 Carrère, L. and Lyard, F.: Modeling the Barotropic Response of the Global Ocean to Atmospheric Wind and Pressure Forcing - Comparisons with Observations, *Geophysical Research Letters*, 30, <https://doi.org/10.1029/2002GL016473>, 2003.
- Cazenave, A., Gouzenes, Y., Birol, F., Leger, F., Passaro, M., Calafat, F. M., Shaw, A., Nino, F., Legeais, J. F., Oelmann, J., Restano, M., and Benveniste, J.: Sea Level along the World’s Coastlines Can Be Measured by a Network of Virtual Altimetry Stations, *Commun Earth Environ*, 3, 1–9, <https://doi.org/10.1038/s43247-022-00448-z>, 2022.
- 745 Chen, W.-W. and Chang, H.-K.: Estimation of Shoreline Position and Change from Satellite Images Considering Tidal Variation, *Estuarine, Coastal and Shelf Science*, 84, 54–60, <https://doi.org/10.1016/j.ecss.2009.06.002>, 2009.
- Cheng, Y., Andersen, O. B., and Knudsen, P.: Integrating Non-Tidal Sea Level Data from Altimetry and Tide Gauges for Coastal Sea Level Prediction, *Advances in Space Research*, 50, 1099–1106, <https://doi.org/10.1016/j.asr.2011.11.016>, 2012.
- 750 Cipollini, P., Calafat, F. M., Jevrejeva, S., Melet, A., and Prandi, P.: Monitoring Sea Level in the Coastal Zone with Satellite Altimetry and Tide Gauges, *Surv Geophys*, 38, 33–57, <https://doi.org/10.1007/s10712-016-9392-0>, 2017.
- Cooper, J. A. G. and Pilkey, O. H.: Sea-Level Rise and Shoreline Retreat: Time to Abandon the Bruun Rule, *Global and Planetary Change*, 43, 157–171, <https://doi.org/10.1016/j.gloplacha.2004.07.001>, 2004.
- D’Anna, M., Idier, D., Castelle, B., Vitousek, S., and Le Cozannet, G.: Reinterpreting the Bruun Rule in the Context of Equilibrium Shoreline Models, *Journal of Marine Science and Engineering*, 9, 974, <https://doi.org/10.3390/jmse9090974>, 2021.
- 755 de Graaf, H., Oude Elberink, S., Bollweg, A., Brügelmann, R., and Richardson, L.: Inwinning “Droge” JARKUS Profielen Langs Nederlandse Kust. Rapportnummer: AGI-GAM-2003-40, 2003.
- Delft, T.: Site Information for Terschelling, <http://gnss1.tudelft.nl/dpga/station/Terschelling.html>, 2022.
- Dettmering, D., Müller, F. L., Oelmann, J., Passaro, M., Schwatke, C., Restano, M., Benveniste, J., and Seitz, F.: North SEAL: A New Dataset of Sea Level Changes in the North Sea from Satellite Altimetry, *Earth System Science Data*, 13, 3733–3753, <https://doi.org/10.5194/essd-13-3733-2021>, 2021.
- 760 DGFI: OpenADB, ALES Sea Surface Heights, <https://openadb.dgfi.tum.de/en/products/adaptive-leading-edge-subwaveform-retracker/>, 2023.
- Do, A. T., de Vries, S., and Stive, M. J.: The Estimation and Evaluation of Shoreline Locations, Shoreline-Change Rates, and Coastal Volume Changes Derived from Landsat Images, *Journal of Coastal Research*, 35, 56, <https://doi.org/10.2112/JCOASTRES-D-18-00021.1>, 2019.
- 765 Eleveld, M. A., van der Wal, D., and van Kessel, T.: Estuarine Suspended Particulate Matter Concentrations from Sun-Synchronous Satellite Remote Sensing: Tidal and Meteorological Effects and Biases, *Remote Sensing of Environment*, 143, 204–215, <https://doi.org/10.1016/j.rse.2013.12.019>, 2014.
- Fokker, P. A., van Leijen, F. J., Orlic, B., van der Marel, H., and Hanssen, R. F.: Subsidence in the Dutch Wadden Sea, *Netherlands Journal of Geosciences*, 97, 129–181, <https://doi.org/10.1017/njg.2018.9>, 2018.
- 770 Gazeaux, J., Williams, S., King, M., Bos, M., Dach, R., Deo, M., Moore, A. W., Ostini, L., Petrie, E., Roggero, M., Teferle, F. N., Olivares, G., and Webb, F. H.: Detecting Offsets in GPS Time Series: First Results from the Detection of Offsets in GPS Experiment, *Journal of Geophysical Research: Solid Earth*, 118, 2397–2407, <https://doi.org/10.1002/jgrb.50152>, 2013.



- Gravelle, M., Wöppelmann, G., Gobron, K., Altamimi, Z., Guichard, M., Herring, T., and Rebischung, P.: The ULR-repro3 GPS Data
775 Reanalysis and Its Estimates of Vertical Land Motion at Tide Gauges for Sea Level Science, *Earth System Science Data*, 15, 497–509,
<https://doi.org/10.5194/essd-15-497-2023>, 2023.
- Hagenaars, G., de Vries, S., Luijendijk, A. P., de Boer, W. P., and Reniers, A. J. H. M.: On the Accuracy of Automated Shoreline Detec-
tion Derived from Satellite Imagery: A Case Study of the Sand Motor Mega-Scale Nourishment, *Coastal Engineering*, 133, 113–125,
<https://doi.org/10.1016/j.coastaleng.2017.12.011>, 2018.
- 780 Hart-Davis, M. G., Piccioni, G., Dettmering, D., Schwatke, C., Passaro, M., and Seitz, F.: EOT20: A Global Ocean Tide Model from Multi-
Mission Satellite Altimetry, *Earth System Science Data*, 13, 3869–3884, <https://doi.org/10.5194/essd-13-3869-2021>, 2021.
- Hart-Davis, M. G., Laan, S., Schwatke, C., Backeberg, B., Dettmering, D., Zijl, F., Verlaan, M., Passaro, M., and Seitz, F.: Altimetry-Derived
Tide Model for Improved Tide and Water Level Forecasting along the European Continental Shelf, *Ocean Dynamics*, 73, 475–491,
<https://doi.org/10.1007/s10236-023-01560-0>, 2023.
- 785 Hermans, T. H. J., Gregory, J. M., Palmer, M. D., Ringer, M. A., Katsman, C. A., and Slagen, A. B. A.: Projecting Global Mean Sea-Level
Change Using CMIP6 Models, *Geophysical Research Letters*, 48, e2020GL092064, <https://doi.org/10.1029/2020GL092064>, 2021.
- Hersbach, H., Bell, B., Berrisford, P., Biavati, G., Horányi, A., Muñoz Sabater, J., Nicolas, J., Peubey, C., Radu, R., Rozum, I., Schep-
ers, D., Simmons, A., Soci, C., Dee, D., and Thépaut, J.-N.: ERA5 Monthly Averaged Data on Single Levels from 1959 to Present,
<https://doi.org/10.24381/CDS.F17050D7>, 2022.
- 790 Hinkel, J., Lincke, D., Vafeidis, A. T., Perrette, M., Nicholls, R. J., Tol, R. S. J., Marzeion, B., Fettweis, X., Ionescu, C.,
and Levermann, A.: Coastal Flood Damage and Adaptation Costs under 21st Century Sea-Level Rise, *PNAS*, 111, 3292–3297,
<https://doi.org/10.1073/pnas.1222469111>, 2014.
- Holgate, S. J., Matthews, A., Woodworth, P. L., Rickards, L. J., Tamisiea, M. E., Bradshaw, E., Foden, P. R., Gordon, K. M., Jevrejeva, S.,
and Pugh, J.: New Data Systems and Products at the Permanent Service for Mean Sea Level, *Journal of Coastal Research*, 29, 493–504,
795 <http://www.psmsl.org/data/obtaining/>, 2013.
- Hooijer, A. and Vernimmen, R.: Global LiDAR Land Elevation Data Reveal Greatest Sea-Level Rise Vulnerability in the Tropics, *Nature
Communications*, 12, 3592, <https://doi.org/10.1038/s41467-021-23810-9>, 2021.
- Jordan, C., Visscher, J., and Schlurmann, T.: Projected Responses of Tidal Dynamics in the North Sea to Sea-Level Rise and Morphological
Changes in the Wadden Sea, *Frontiers in Marine Science*, 8, <https://www.frontiersin.org/article/10.3389/fmars.2021.685758>, 2021.
- 800 Karegar, M. A., Larson, K. M., Kusche, J., and Dixon, T. H.: Novel Quantification of Shallow Sediment Compaction by GPS
Interferometric Reflectometry and Implications for Flood Susceptibility, *Geophysical Research Letters*, 47, e2020GL087807,
<https://doi.org/10.1029/2020GL087807>, 2020.
- Kleinherenbrink, M., Riva, R., and Frederikse, T.: A Comparison of Methods to Estimate Vertical Land Motion Trends from GNSS and
Altimetry at Tide Gauge Stations, *Ocean Science*, 14, 187–204, <https://doi.org/10.5194/os-14-187-2018>, 2018.
- 805 Larson, M. and Kraus, N. C.: Temporal and Spatial Scales of Beach Profile Change, Duck, North Carolina, *Marine Geology*, 117, 75–94,
[https://doi.org/10.1016/0025-3227\(94\)90007-8](https://doi.org/10.1016/0025-3227(94)90007-8), 1994.
- Le Cozannet, G., Garcin, M., Yates, M., Idier, D., and Meyssignac, B.: Approaches to Evaluate the Recent Impacts of Sea-Level Rise on
Shoreline Changes, *Earth-Science Reviews*, 138, 47–60, <https://doi.org/10.1016/j.earscirev.2014.08.005>, 2014.
- Liu, H., Sherman, D., and Gu, S.: Automated Extraction of Shorelines from Airborne Light Detection and Ranging Data and Accuracy
810 Assessment Based on Monte Carlo Simulation, *Journal of Coastal Research*, 236, 1359–1369, <https://doi.org/10.2112/05-0580.1>, 2007.



- Luijendijk, A., Hagenaaars, G., Ranasinghe, R., Baart, F., Donchyts, G., and Aarninkhof, S.: The State of the World's Beaches, *Scientific Reports*, 8, 6641, <https://doi.org/10.1038/s41598-018-24630-6>, 2018.
- Lyard, F. H., Allain, D. J., Cancet, M., Carrère, L., and Picot, N.: FES2014 Global Ocean Tide Atlas: Design and Performance, *Ocean Sci.*, 17, 615–649, <https://doi.org/10.5194/os-17-615-2021>, 2021.
- 815 Mangini, F., Chafik, L., Bonaduce, A., Bertino, L., and Nilsen, J. E. Ø.: Sea-Level Variability and Change along the Norwegian Coast between 2003 and 2018 from Satellite Altimetry, Tide Gauges, and Hydrography, *Ocean Science*, 18, 331–359, <https://doi.org/10.5194/os-18-331-2022>, 2022.
- Minneboo, F. A. J.: Richtlijnen voor de inwinning, bewerking en opslag van gegevens van jaarlijkse kustmetingen. rapport RIKZ-95.022, 1995.
- 820 Morrow, R., Blurmstein, D., and Dibarboure, G.: Fine-Scale Altimetry and the Future SWOT Mission, *New Frontiers in Operational Oceanography*, pp. 191–226, <https://fsu.digital.flvc.org/islandora/object/fsu%3A602135/>, 2018.
- Morton, R. A., Miller, T., and Moore, L.: Historical Shoreline Changes Along the US Gulf of Mexico: A Summary of Recent Shoreline Comparisons and Analyses, *Journal of Coastal Research*, 214, 704–709, <https://doi.org/10.2112/04-0230.1>, 2005.
- Nicolae Lerma, A., Castelle, B., Marieu, V., Robinet, A., Bulteau, T., Bernon, N., and Mallet, C.: Decadal Beach-Dune Profile Monitoring along a 230-Km High-Energy Sandy Coast: Aquitaine, Southwest France, *Applied Geography*, 139, 102645, <https://doi.org/10.1016/j.apgeog.2022.102645>, 2022.
- 825 Oelsmann, J., Passaro, M., Dettmering, D., Schwatke, C., Sánchez, L., and Seitz, F.: The Zone of Influence: Matching Sea Level Variability from Coastal Altimetry and Tide Gauges for Vertical Land Motion Estimation, *Ocean Science*, 17, 35–57, <https://doi.org/10.5194/os-17-35-2021>, 2021.
- 830 Parker, B. B.: The Difficulties in Measuring a Consistently Defined Shoreline—The Problem of Vertical Referencing, *Journal of Coastal Research*, pp. 44–56, <https://www.jstor.org/stable/25736599>, 2003.
- Passaro, M.: COSTA v1.0: DGFI-TUM Along Track Sea Level Product for ERS-2 and Envisat (1996-2010) in the Mediterranean Sea and in the North Sea, *Links to Data Sets in NetCDF Format*, <https://doi.org/10.1594/PANGAEA.871920>, 2017.
- Passaro, M., Cipollini, P., Vignudelli, S., Quartly, G. D., and Snaith, H. M.: ALES: A Multi-Mission Adaptive Subwaveform Retracker for Coastal and Open Ocean Altimetry, *Remote Sensing of Environment*, 145, 173–189, <https://doi.org/10.1016/j.rse.2014.02.008>, 2014.
- 835 Passaro, M., Fenoglio-Marc, L., and Cipollini, P.: Validation of Significant Wave Height From Improved Satellite Altimetry in the German Bight, *IEEE Transactions on Geoscience and Remote Sensing*, 53, 2146–2156, <https://doi.org/10.1109/TGRS.2014.2356331>, 2015.
- Pawlowicz, R., Beardsley, B., and Lentz, S.: Classical Tidal Harmonic Analysis Including Error Estimates in MATLAB Using T_TIDE, *Computers & Geosciences*, 28, 929–937, [https://doi.org/10.1016/S0098-3004\(02\)00013-4](https://doi.org/10.1016/S0098-3004(02)00013-4), 2002.
- 840 Pfeffer, J. and Allemand, P.: The Key Role of Vertical Land Motions in Coastal Sea Level Variations: A Global Synthesis of Multisatellite Altimetry, Tide Gauge Data and GPS Measurements, *Earth and Planetary Science Letters*, 439, 39–47, <https://doi.org/10.1016/j.epsl.2016.01.027>, 2016.
- Piccioni, G., Dettmering, D., Passaro, M., Schwatke, C., Bosch, W., and Seitz, F.: Coastal Improvements for Tide Models: The Impact of ALES Retracker, *Remote Sensing*, 10, 700, <https://doi.org/10.3390/rs10050700>, 2018.
- 845 Ponte, R. M.: Low-Frequency Sea Level Variability and the Inverted Barometer Effect, *Journal of Atmospheric and Oceanic Technology*, 23, 619–629, <https://doi.org/10.1175/JTECH1864.1>, 2006.
- Pot, R.: Coastal Morphologic Data: Yearly Coastal Survey in the Netherlands. JARKUS Systematics and Accuracy. Part of M.Sc. Thesis System-description Noord-Holland Coast and a Review of the Current Nourishment Strategy Applied., Ph.D. thesis, TU Delft, 2011.



- Quataert, E., Oost, A., Hijma, M., and Elias, E.: Beheerbibliotheek Terschelling, 2020.
- 850 Ridderinkhof, W., Hoekstra, P., van der Vegt, M., and de Swart, H. E.: Cyclic Behavior of Sandy Shoals on the Ebb-Tidal Deltas of the Wadden Sea, *Continental Shelf Research*, 115, 14–26, <https://doi.org/10.1016/j.csr.2015.12.014>, 2016.
- Rijkswaterstaat: JARKUS Dataset, <https://opendap.deltares.nl/thredds/fileServer/opendap/rijkswaterstaat/jarkus/profiles/transect.nc>, 2022a.
- Rijkswaterstaat, D. M. o. I. a. W. M.: Waterhoogte Oppervlaktewater t.o.v. Normaal Amsterdams Peil in Cm, <https://waterinfo.rws.nl/>, 2022b.
- Roberts, J. and Roberts, T. D.: Use of the Butterworth Low-Pass Filter for Oceanographic Data, *J. Geophys. Res.*, 83, 5510, 855 <https://doi.org/10.1029/JC083iC11p05510>, 1978.
- Robertson, V. W., Whitman, D., Zhang, K., and Leatherman, S. P.: Mapping Shoreline Position Using Airborne Laser Altimetry, *Journal of Coastal Research*, 20, 884–892, [https://doi.org/10.2112/1551-5036\(2004\)20\[884:MSPUAL\]2.0.CO;2](https://doi.org/10.2112/1551-5036(2004)20[884:MSPUAL]2.0.CO;2), 2004.
- Santamaría-Gómez, A., Gravelle, M., Collilieux, X., Guichard, M., Míguez, B. M., Tiphaneau, P., and Wöppelmann, G.: Mitigating the Effects of Vertical Land Motion in Tide Gauge Records Using a State-of-the-Art GPS Velocity Field, *Global and Planetary Change*, 860 98–99, 6–17, <https://doi.org/10.1016/j.gloplacha.2012.07.007>, 2012.
- Schuerch, M., Spencer, T., Temmerman, S., Kirwan, M. L., Wolff, C., Lincke, D., McOwen, C. J., Pickering, M. D., Reef, R., Vafeidis, A. T., Hinkel, J., Nicholls, R. J., and Brown, S.: Future Response of Global Coastal Wetlands to Sea-Level Rise, *Nature*, 561, 231–234, <https://doi.org/10.1038/s41586-018-0476-5>, 2018.
- Shirzaei, M., Freymueller, J., Törnqvist, T. E., Galloway, D. L., Dura, T., and Minderhoud, P. S. J.: Measuring, Modelling and Projecting 865 Coastal Land Subsidence, *Nat Rev Earth Environ*, 2, 40–58, <https://doi.org/10.1038/s43017-020-00115-x>, 2021.
- Simon, K. M., Riva, R. E. M., Kleinherenbrink, M., and Frederikse, T.: The Glacial Isostatic Adjustment Signal at Present Day in Northern Europe and the British Isles Estimated from Geodetic Observations and Geophysical Models, *Solid Earth*, 9, 777–795, <https://doi.org/10.5194/se-9-777-2018>, 2018.
- SONEL: GNSS Data, <https://www.sonel.org/?page=gps&idStation=2035>, 2022.
- 870 Stockdonf, H. F., Jr., A. H. S., List, J. H., and Holman, R. A.: Estimation of Shoreline Position and Change Using Airborne Topographic Lidar Data, *Journal of Coastal Research*, 18, 502–513, <http://www.jstor.org/stable/4299097>, 2002.
- Turner, I. L., Harley, M. D., Short, A. D., Simmons, J. A., Bracs, M. A., Phillips, M. S., and Splinter, K. D.: A Multi-Decade Dataset of Monthly Beach Profile Surveys and Inshore Wave Forcing at Narrabeen, Australia, *Sci Data*, 3, 160024, <https://doi.org/10.1038/sdata.2016.24>, 2016.
- 875 van IJendoorn, C.: Jarkus Analysis Toolbox (JAT), <https://github.com/christavaniijendoorn/JAT>, 2022.
- Vermeersen, B. L., Slangen, A. B., Gerkema, T., Baart, F., Cohen, K. M., Dangendorf, S., Duran-Matute, M., Frederikse, T., Grinsted, A., Hijma, M. P., Jevrejeva, S., Kiden, P., Kleinherenbrink, M., Meijles, E. W., Palmer, M. D., Rietbroek, R., Riva, R. E., Schulz, E., Slobbe, D. C., Simpson, M. J., Sterlini, P., Stocchi, P., van de Wal, R. S., and van der Wegen, M.: Sea-Level Change in the Dutch Wadden Sea, *Netherlands Journal of Geosciences*, 97, 79–127, <https://doi.org/10.1017/njg.2018.7>, 2018.
- 880 Vignudelli, S., Kostianoy, A. G., Cipollini, P., and Benveniste, J., eds.: *Coastal Altimetry*, Springer Berlin Heidelberg, Berlin, Heidelberg, <https://doi.org/10.1007/978-3-642-12796-0>, 2011.
- Vignudelli, S., Birol, F., Benveniste, J., Fu, L.-L., Picot, N., Raynal, M., and Roinard, H.: Satellite Altimetry Measurements of Sea Level in the Coastal Zone, *Surv Geophys*, 40, 1319–1349, <https://doi.org/10.1007/s10712-019-09569-1>, 2019.
- Vos, K., Harley, M. D., Splinter, K. D., Simmons, J. A., and Turner, I. L.: Sub-Annual to Multi-Decadal Shoreline Variability from Publicly 885 Available Satellite Imagery, *Coastal Engineering*, 150, 160–174, <https://doi.org/10.1016/j.coastaleng.2019.04.004>, 2019a.



- Vos, K., Splinter, K. D., Harley, M. D., Simmons, J. A., and Turner, I. L.: CoastSat: A Google Earth Engine-enabled Python Toolkit to Extract Shorelines from Publicly Available Satellite Imagery, *Environmental Modelling & Software*, 122, 104528, <https://doi.org/10.1016/j.envsoft.2019.104528>, 2019b.
- 890 Voudoukas, M. I., Ranasinghe, R., Mentaschi, L., Plomaritis, T. A., Athanasiou, P., Luijendijk, A., and Feyen, L.: Sandy Coastlines under Threat of Erosion, *Nat. Clim. Chang.*, 10, 260–263, <https://doi.org/10.1038/s41558-020-0697-0>, 2020.
- Wang, Z. B., Hoekstra, P., Burchard, H., Ridderinkhof, H., De Swart, H. E., and Stive, M. J. F.: Morphodynamics of the Wadden Sea and Its Barrier Island System, *Ocean & Coastal Management*, 68, 39–57, <https://doi.org/10.1016/j.ocecoaman.2011.12.022>, 2012.
- Wiegmann, N., Perluka, R., and Boogaard, K.: Onderzoek naar efficiency verbetering kustlodingen. Rapportnummer: AGI/110105/GAM010, 2002.
- 895 Wöppelmann, G. and Marcos, M.: Vertical Land Motion as a Key to Understanding Sea Level Change and Variability, *Reviews of Geophysics*, 54, 64–92, <https://doi.org/10.1002/2015RG000502>, 2016.
- Yousef, A. H., Iftekharuddin, K. M., and Karim, M. A.: Shoreline Extraction from Light Detection and Ranging Digital Elevation Model Data and Aerial Images, *OE*, 53, 011 006, <https://doi.org/10.1117/1.OE.53.1.011006>, 2013.